



HAL
open science

Present-day gully activity in Sisyphi Cavi, Mars -Flow-like features and block movements

Jan Raack, Susan J. Conway, Thomas Heyer, Valentin Tertius Bickel, Meven
Philippe, Harald Hiesinger, Andreas Johnsson, Marion Massé

► To cite this version:

Jan Raack, Susan J. Conway, Thomas Heyer, Valentin Tertius Bickel, Meven Philippe, et al.. Present-day gully activity in Sisyphi Cavi, Mars -Flow-like features and block movements. *Icarus*, 2020, 350, pp.113899. 10.1016/j.icarus.2020.113899 . hal-02989781

HAL Id: hal-02989781

<https://hal.science/hal-02989781>

Submitted on 5 Nov 2020

HAL is a multi-disciplinary open access archive for the deposit and dissemination of scientific research documents, whether they are published or not. The documents may come from teaching and research institutions in France or abroad, or from public or private research centers.

L'archive ouverte pluridisciplinaire **HAL**, est destinée au dépôt et à la diffusion de documents scientifiques de niveau recherche, publiés ou non, émanant des établissements d'enseignement et de recherche français ou étrangers, des laboratoires publics ou privés.

1 **Present-day gully activity in Sisyphi Cavi, Mars – Flow-like features and block movements**

2

3 Jan Raack^a, Susan J. Conway^b, Thomas Heyer^a, Valentin T. Bickel^{c,d}, Meven Philippe^b, Harald
4 Hiesinger^a, Andreas Johnsson^e, Marion Massé^b

5

6 ^aInstitut für Planetologie, Westfälische Wilhelms-Universität Münster, Wilhelm-Klemm-Str. 10,
7 48149 Münster, Germany

8 ^bLaboratoire de Planétologie et Géodynamique, UMR 6112, CNRS, Université de Nantes, 2
9 chemin de la Houssinière, BP 92205, 44322 Nantes Cedex 3, France

10 ^cDepartment Planets and Comets, Max Planck Institute for Solar System Research, Justus-von-
11 Liebig-Weg 3, 37077 Göttingen, Germany

12 ^dDepartment of Earth Sciences, ETH Zurich, Sonneggstrasse 5, 8092 Zurich, Switzerland

13 ^eDepartment of Earth Sciences, University of Gothenburg, Box 460, Gothenburg SE-405 30,
14 Sweden

15

16 Keywords: Mars; Mars, surface; Geological processes; Photometry; Mars, climate; Mars, polar
17 geology; Ices

18

19

20

21

22

23

24 **Abstract**

25 The continuously increasing number of multi-temporal high-resolution images from the surface of
26 Mars offers the possibility for detailed studies of present-day surface activity. In this study we
27 investigated all gullies in the Sisyphi Cavi region (355° E, 71° S) of the south polar region of Mars.
28 This region is influenced by the seasonal deposition of a decimeters-thick translucent slab ice in
29 late autumn/winter and its subsequent sublimation in spring. We mapped all gullies (n = 17.760)
30 and measured their orientations. We also identified gullies with contemporary activity (n = 35)
31 using multi-temporal HiRISE images for martian years (MY) 28 to 34. We observed two different
32 kinds of activity: (1) dark flow-like features, and (2) movement of blocks. For both, sediment was
33 transported from the source region (alcove and/or flanks of channels) down the gully. Using image
34 data from HRSC, CTX, and HiRISE, we monitored the general defrosting of the study region. We
35 also analyzed the maximum daytime surface temperatures of the complete study region based on
36 TES data from MYs 24 to 26. To identify the origin and triggering mechanism of the observed
37 activity, we used: (1) detailed topographic investigations (e.g., slope angles) of two extensively
38 gullied slopes based on two HiRISE-DTMs, (2) identification of small scale displacements with
39 Digital Image Correlation (DIC), and (3) orientation measurements of active gullies and
40 comparison to non-active gullies.

41 We found that for the active gullies studied, activity happens at the end of spring between $L_s \sim 225^\circ$
42 and $\sim 250^\circ$. This is consistent with the timing of final stages of defrosting in the region. At this
43 time, some surfaces are already defrosted while others still host the seasonal slab ice cover. For
44 the surfaces with slab ice, dark defrosting spots (and flows, if the surface is inclined) are observed
45 on dark dunes as well as on gully aprons and in gully channels. These spots form when, triggered
46 by basal sublimation generated overpressure, sediment entrained in CO_2 -gas is transported through

47 cracks within the ice and redeposited onto the frosted surface. We compared and linked both
48 morphologic features (dark dune spots and dark flow-like features) and concluded that these
49 features have comparable or even the same triggering mechanisms. Based on this extensive study,
50 the most plausible mechanism for ongoing gully activity can be divided into two steps: 1)
51 accumulation of material within gully channels via small dry flows on top of the slab ice
52 (comparable to dark dune spots/flows), 2) when a critical mass is reached, the sediment flows
53 down the still frosted gully on top of the sublimating ice or as a mixture of dry material and ice in
54 a catastrophic flow. The triggering factor for the movement of blocks remains unclear, as their
55 timing could not be constrained with the available data. We identified headwall erosion in one
56 gully in the study region, whereas a discrete source could not be identified for the other sites,
57 suggesting multiple failure mechanisms could be active in such gullies. Finally, through volume
58 balance calculations we show that active gullies in Sisyphi Cavi could have been formed within
59 decades to several tens of thousands of MY, but gully-morphology indicates a much-longer period
60 for formation of the entire gully-landform.

61

62 **Introduction**

63 Gullies on Mars are features comprised of an alcove, channel, and debris apron and can range up
64 to several kilometers in length (Malin and Edgett, 2000; Figure 1). They are found on steep slopes
65 in the mid to high latitudes of Mars and have a wide range of morphologies (e.g., Dickson et al.,
66 2007; Dickson and Head, 2009; Conway et al., 2011, 2015; Harrison et al., 2015). They were
67 initially thought to originate from erosion and deposition of sediments by flowing liquid water, in
68 a similar fashion to gullies on Earth (Malin and Edgett, 2000).

69 An alternate hypothesis, proposed shortly after the discovery of gullies, is that CO₂ could play a
70 role in triggering sediment motion that forms gullies (Musselwhite et al., 2001; Hoffman, 2002).
71 CO₂ ice is deposited on the martian surface every winter, forming a continuous layer down to ~50°
72 in both hemispheres and a discontinuous layer down to ~30° latitude (Piqueux et al., 2003;
73 Schorghofer and Edgett, 2006; Vincendon et al., 2010a, 2010b; Pilorget et al., 2011) mirroring the
74 latitudinal distribution of gullies. The CO₂ hypothesis was initially proposed based on the presence
75 of gullies located near the south pole of Mars where annual CO₂ frost deposits would be at their
76 thickest (Hoffman, 2002; Ishii and Sasaki, 2004; Cedillo-Flores et al., 2011) and where surface
77 temperatures are too low to support the presence of liquid water. The mechanism proposed by
78 Hoffman et al. (2002) was that liquid CO₂ outbursts were responsible for gullies here, but the
79 stability of liquid CO₂ on Mars means its presence is even more unlikely than liquid water (Stewart
80 and Nimmo, 2002). Ishii and Sasaki (2004) and Ishii et al. (2006) proposed that gullies could be
81 formed by CO₂ ice avalanches and Hugenholtz (2008) slightly modified this idea by suggesting
82 CO₂ ice coated grains could avalanche by vaporization of the CO₂ frost. Cedillo-Flores et al. (2011)
83 proposed a mechanism by which dust or sand superposed onto a CO₂ ice surface would be
84 mobilized by sublimation of the underlying CO₂ ice. Pilorget and Forget (2016) suggested that
85 martian gullies could result from basal CO₂ sublimation of an ice layer and subsequent movement
86 of material underneath the CO₂ ice layer.

87 Ongoing observations of gully activity at the present-day have continued to raise questions, not
88 only regarding the formation mechanisms of gullies, but also the triggering mechanisms of the
89 activity (Malin et al., 2006; McEwen et al., 2007a; Diniega et al., 2010; Dundas et al., 2010, Reiss
90 et al., 2010, Dundas et al., 2012; Jouannic et al., 2012; Dundas et al., 2015; Raack et al., 2015;
91 Pasquon et al., 2016; Dundas et al., 2019; Pasquon et al., 2019a, 2019b). Recent laboratory

92 experiments under martian atmospheric conditions have shown that unstable water on the martian
93 surface could have an influence on the formation of recent and present-day mass wasting features
94 (Raack et al., 2017; HERNY et al., 2019), but the climatic conditions (e.g., low surface temperatures)
95 at times when gully activity occurs on Mars makes water-triggered activity very unlikely. As a
96 consequence, the focus of research has moved from H₂O- to CO₂-related mechanisms when
97 investigating contemporary gully activity, but all three possible triggering factors (H₂O, CO₂ and
98 dry or possible combinations) should continue to be considered for active gullies on Mars.

99 This study focuses on polar pit gullies, which were the focus of the initial studies referring to CO₂
100 frost as the mechanism behind martian gullies. Our objective is to exploit all available imaging
101 data to identify and catalogue the types, timing, and frequency of present-day activity in these
102 gullies with the aim to provide insights into the processes driving this activity. We also investigate
103 whether the present-day processes could account for the presence and morphology of all the gullies
104 in the south-polar pits or whether other mechanisms need to be invoked. Furthermore, the polar
105 location of the gullies investigated in this study combined with the polar orbits of the main imaging
106 orbiters means that there is a higher frequency of observations compared to gullies at lower
107 latitudes, providing a unique opportunity to study the activity of gullies in detail.



108

109 **Figure 1:** (a) Color and Stereo Surface Imaging System (CaSSIS) image (Thomas et al., 2017) of
 110 a gullied slope within the study region. The gullies are the same as those presented in Figure 14.

111 Bright surfaces correspond to the annually deposited CO₂ surface frost cover. This image was
 112 acquired at the end of spring when the general defrosting of the study region was already well-
 113 advanced. CO₂ surface frosts are only visible on the large dark dune, which is completely covered
 114 with a bright ice cover, and on gully aprons / alcoves. Dark spots on the dune show slight flow-
 115 like streaks where the slope is highest (on the lower part of the dune). Image
 116 (MY34_003464_256_1) was acquired in MY 34 at Ls 242°, flow direction is from top to bottom.

117 (b) Context image of the complete gullied region (Region 5, see Figure 2). Image was acquired in
 118 MY 30 at Ls 201° (CTX-image G06_020600_1115) where surface frost covers the complete
 119 region and first dark spots on the dune and defrosting of gully alcoves at the north-facing (equator-
 120 facing) slope are visible. The black frame represents the location of the CaSSIS image.

121

122

123

124 **1. Study region**

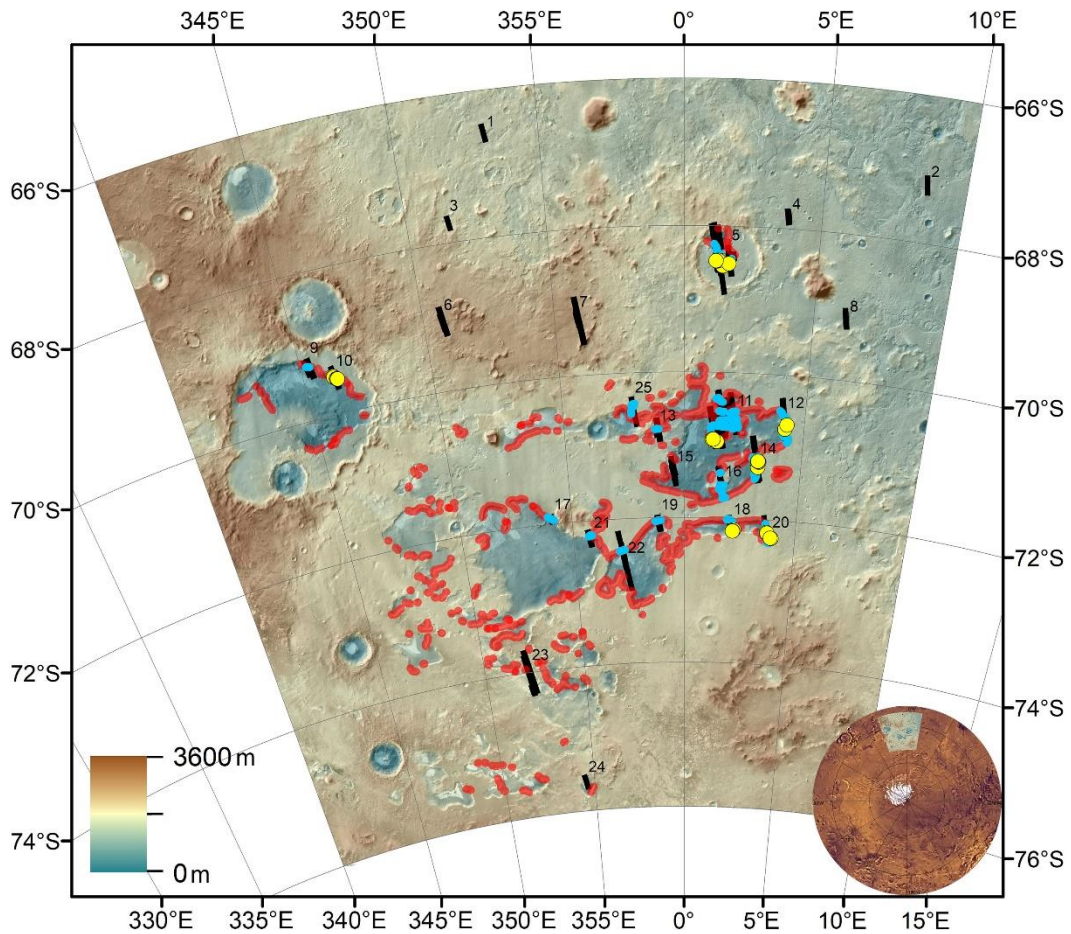
125 The study region comprises the complete Sisyphi Cavi region, an area with numerous polar pits
126 (depressions) up to ~1 km deep (Tanaka and Scott, 1987). Sisyphi Cavi is named after “Sisyphus”,
127 the ancient king of Ephyra. In Greek mythology, Sisyphus was punished in the underworld after
128 his death. He had to roll a large boulder up a steep hill, but each time just before reaching the top
129 of the hill, the boulder would roll down again and he would have to start again. This frustrating
130 punishment including rolling boulders turns out to be surprisingly relevant to this work and shows
131 the name was well-chosen (see Section 3.1.2).

132 The formation of these irregular steep-sided polar pits in general and specifically in this region is
133 not well understood. The pits are incised into relatively smooth upland surfaces of Amazonian age
134 (Tanaka and Scott, 1987) and some layering is visible at their slopes. There are two large regions
135 with polar pitted terrain (Angusti Cavi at ~290° E and ~77° S; Sisyphi Cavi at ~355° E and ~71°
136 S) near the south pole, which were first noticed on Mariner 9 images and described by Murray et
137 al. (1972) and Sharp (1973) as eolian erosion (denudation) of sedimentary rocks of eolian or
138 volcanic origin. Later, Howard (1981) raised the hypothesis that basal melting of ground ice
139 formed these pits, which was supported by Thomas et al. (1992) who reported that the region
140 consists of volatile-rich polar cap deposits, and by Head (2000) and Ghatan and Head (2002). The
141 basal melting is believed to have been brought about by increased geothermal heat flux in the
142 vicinity of subglacial volcanoes located in the eastern part of Sisyphi Cavi (Ghatan and Head,
143 2002).

144 No matter of their origin, the pits of the Sisyphi Cavi form steep slopes in the polar regions. Gullies
145 form preferentially on steep slopes (Conway et al., 2019) so this is one of two polar concentrations
146 of gullies in the southern hemisphere, the other being Angusti Cavi. We defined our study region

147 from -66° to -76° S and from 340° to 10° E in which nearly all the pits in Sisyphi Cavi were
148 covered (Figure 2). Raack et al. (2015) were the first to study the activity of gullies in Sisyphi Cavi
149 in detail. One of their gullies showed signs of activity every Mars year (MY) during their
150 observation phase between MYs 29 and 31 and was analyzed in detail. Raack et al. (2015) found
151 that sediments were transported down the gully and deposited over and next to the apron. Gully
152 activity appeared during mid-spring when surface temperatures began to rise and the seasonal
153 surface ice sublimated. Based on spectral observations and numerical modeling, the surface ice
154 was identified as CO_2 translucent slab ice with minor contaminations of H_2O ice. The most
155 plausible mechanism for the observed activity were dry flows mobilized over the sublimating CO_2
156 ice surface (e.g., Cedillo-Flores et al., 2011). The material for the dry flows was most likely to
157 originate from the slopes of the gully channel, triggered by sublimation. Our here presented work
158 includes the active gully analyzed by Raack et al. (2015) and adds new insights based on newly
159 available high-resolution datasets.

160 Studies of gully activity by Dundas et al. (2012, 2015, 2019) also included the Sisyphi Cavi gullies.
161 Dundas et al. (2012, 2015, 2019) noted activity in them but made no detailed specific morphologic
162 observations. In a study of the topographic long profiles of gullies on Mars, Conway et al. (2015)
163 found that gullies in the polar pits had shallower slopes than those elsewhere and that they had
164 generally a more pronounced curvature. Gullies in Sisyphi Cavi can be named to be “classic
165 gullies” with a distinct alcove, channel, and apron system.



166

167 **Figure 2:** THEMIS-IR data superposed by a MOLA digital terrain model (DTM) of the study
 168 region, which comprises the complete Sisyphi Cavi region. Multi-temporal HiRISE image
 169 footprints are represented by black rectangles, numbered from north (1) to south (24), except (25)
 170 because these multi-temporal datasets were acquired after the begin of our study. These footprints
 171 (25) can be found in the middle of the study region. These numbers represent the 25 individual
 172 multi-temporal covered study regions which were investigated. Gully activity was found in seven
 173 of them (5, 10, 11, 12, 14, 18, 20, see yellow dots). Red dots represent mapped gullies based on
 174 CTX imagery (n = 17,760), blue dots represent mapped gullies on multi-temporal HiRISE imagery
 175 (n = 2,067), yellow dots represent contemporary active gullies (n = 35) identified on multi-
 176 temporal HiRISE images.

177 2. Data and methods

178 2.1. Datasets

179 We used different visual and thermal datasets for our study of active gullies and the defrosting
180 within the study region. For a general overview, context, and topographic information, we used
181 Thermal Emission Imaging System daytime infrared (THEMIS-IR) (Christensen et al., 2004) data
182 combined with a Mars Orbiter Laser Altimeter digital terrain model (MOLA DTM) (Zuber et al.,
183 1992). MOLA polar gridded data (460 m/pix) were used for slope orientation measurements.
184 Furthermore, 28 High Resolution Stereo Camera (HRSC) images (at approximately 12.5 m/pixel,
185 Jaumann et al., 2007) were also used for a general overview of the study region and for frost
186 identification during spring, as a validation of observations with the Context Camera (CTX). CTX
187 images (Malin et al., 2007) were used for mapping and orientation measurements of all gullies and
188 gullied slopes, as well as for identification of defrosting in the entire study region. We used 382
189 CTX images with a resolution of ~5 m/pixel. Furthermore, we used a CTX mosaic provided by
190 Dickson et al. (2018) as a basis for the mapping of all gullies in the study region. For detailed and
191 multi-temporal investigations, we analyzed 212 multi-temporal (with a coverage of at least two
192 images of same area) High Resolution Imaging Science Experiment (HiRISE) images with a
193 resolution between 0.25 and 1 m/pixel (McEwen et al., 2007b). Two Colour and Stereo Surface
194 Imaging System (CaSSIS) images (Thomas et al., 2017) were used for a color overview of frost-
195 covered gullied slopes.

196 Visual datasets were identified using the MUTED webtool (Heyer et al., 2018), which provides a
197 direct download link to the PDS Geoscience Node ([http://pds-
198 geosciences.wustl.edu/dataserv/mars.html](http://pds-geosciences.wustl.edu/dataserv/mars.html)). CTX and HiRISE images were downloaded as a pre-
199 processed product for direct integration into an ESRI ArcGIS project. Possible necessary

200 adjustments of the exact location and perfect co-registration of multi-temporal datasets were done
201 manually in ArcGIS. We identified 25 different regions with multi-temporal coverage (see Figure
202 1). In seven of these regions, we identified contemporary gully activity (active mass wasting
203 features within gullies). Furthermore, we undertook detailed analyses of the timing of defrosting
204 within these seven regions and measured the orientations of active mass wasting features on
205 HiRISE images.

206 For thermal investigations, we used data from the Thermal Emission Spectrometer (TES) with a
207 resolution of about 3 km/pixel (Christensen et al., 2001). We used all available daytime surface
208 temperatures, which were collected between ~13:00 and ~15:00 local mean solar time (where
209 maximum surface temperatures occur on Mars), except some data from MY 25. During this year,
210 data were collected during a global martian dust storm that occurred from about end of June to
211 approximately September in 2001
212 (https://www.jpl.nasa.gov/releases/2001/duststorm_010709.html and
213 <https://mars.nasa.gov/resources/7886/dust-storms-of-2001/>). During this time, the instrument was
214 not able to collect reliable data and surface temperatures were not usable for our study.
215 Consequently, we did not take the data from MY 25 at $L_S 185^\circ$ to $L_S 260^\circ$ (~26th June to ~27th
216 October 2001) into account. In general, TES data were acquired in earlier martian years (MY 24
217 to 26) than the identified contemporary activity (MY 28 to 34). However, we assume that large
218 variations of surface temperatures within the observation time of our investigations and in the
219 study region did not occur and that annually temperatures did not show any large variations. TES
220 data were processed and downloaded directly from the TES webpage at the Arizona State
221 University (ASU) (http://tes.asu.edu/data_tool/).

222

223 **2.2. Methods**

224 **2.2.1. Mapping of gullies and slopes**

225 We have mapped all gullies within the study region based on CTX images in order to place our
226 detailed observations in context and assess the representativeness of the HiRISE sampling. In total,
227 17,760 single gullies were identified and marked. Individual gullies were identified by clearly
228 visible alcoves associated with depositional fans, which are the most prominent features of a gully.
229 Channels are more difficult to identify because sometimes their widths are below the resolution of
230 the CTX data used. Hence, some of the identified sites may be relict gullies, lacking channels. We
231 also identified and marked all gullies that were present within the multi-temporal HiRISE imagery
232 (n = 2,067).

233

234 **2.2.2. Multi-temporal analysis**

235 For the identification of areas with both gully activity and high spatial and temporal repeat
236 coverage of high-resolution images, we used the Multi-Temporal Database of Planetary Image
237 Data (MUTED; Heyer et al., 2018). The web-based tool enables users to identify orbital images
238 covering the same surface area on Mars based on user-defined spatial and temporal constraints. In
239 particular, the database was used to find multi-temporal images with a spatial resolution better than
240 15 m/pix (for CTX images) within the area of interest.

241 After the import of multi-temporal HiRISE imagery into an ArcGIS project, we manually
242 georeferenced particular images to get the best visual overlap to identify changes between the
243 images. In a first step, we focused in the comparison of images with similar timings within a year
244 (comparable solar longitudes) and similar solar incidence angles. This was done so as to have
245 comparable shadows on the surface, which makes it easier to identify changes associated with

246 activity and reduces mistakes, e.g., misidentification of shadows at different angles as mass
247 wasting activity. In a second step, we tried to narrow down the timing of activity to a minimum by
248 analyzing images within a year. If these images are available, (sometimes only a few images within
249 several different years are available), we identified the image “before” and “after” the activity
250 happened, which gives us the maximum timing within a year. For this study, we used the layer-
251 based ArcGIS structure to click manually through all available HiRISE images (Figs. 3-7).

252

253 **2.2.3. Slope measurements and topography**

254 Slope measurements of six active gullies based on HiRISE-Digital Terrain Models (HiRISE-
255 DTMs) were conducted (in red, Figure 8). We used one publicly released HiRISE-DTM (HiRISE
256 stereo pair ESP_013097_1115 and ESP_013585_1115) in region 5 (Figure 8b) which was
257 downloaded from the UA-HiRISE webpage (<https://www.uahirise.org/dtm/>) and we processed
258 another HiRISE stereo pair, ESP_023290_1090 and ESP_048608_1090, in region 11 (Figure 8a)
259 with the standard routines in the USGS Integrated Software for Imagers and Spectrometers (ISIS3)
260 and SOCET SET (Kirk et al., 2008). Both DTMs were used to visualize the slope angles of the six
261 active gullies (Figure 8: A, B, F, G, L, N) in comparison with non-active adjacent gullies (Figure
262 8: C, D, E, H, I, J, K, M, O, P). Profile measurements followed the path from the beginning of their
263 alcoves, through their channels, and across their aprons to the termini of the slopes (Figure 8).
264 Vertical exaggeration is about 2.7 in the displayed figures. For a better statistical analysis of all
265 gullies, we calculated the average slope angle of each individual gully separated in segments of
266 100 m (Figure 8 and Supplementary Table 02). With this method, we were able to identify broad
267 trends in the slopes of the gully profiles.

268

269
270
271
272
273
274
275
276
277
278
279
280
281
282
283
284
285
286
287
288
289
290

2.2.4. Orientations

We have undertaken four different measurements of orientations, binned into 10° azimuth intervals: (1) the number of pixels of all gullied slopes identified on CTX imagery (n = 8,303) based on an aspect map derived from a 21-pixel moving window applied to the MOLA polar gridded data at 460 m/pix, (2) all individual gullies (n = 17,760) found on CTX imagery, (3) the number of pixels of all gullied slopes identified on HiRISE imagery (n = 1,430) also based on the same aspect map used for gullied slopes identified on CTX imagery, and (4) all active gullies (n = 35) based on multi-temporal HiRISE imagery (Figure 9). Individual gully orientation measurements were derived from the mapped gully alcoves (as points) and sampling the value directly underneath the point representing the alcoves of the underlying MOLA aspect map. Orientations of active gullies were derived from the long profiles of the gullies they were hosted in and, if possible, from the direct visible path of active dark flow-like feature. The analysis of the gullied and non-gullied slopes was carried out on all pixels with slopes > 6° because this value was the lowest value that reliably captured all the gullied and non-gullied slopes without including parts of the plateaux or pit-floors. Please note that the resolution of the MOLA aspect map smoothed out the gully-alcoves so that it represents the general orientation of the hillslope. The number of pixels of all gullied slopes (1) and (3) were divided by the orientation of all pixels of all slopes (gullied and non-gullied CTX-identified slopes: 43,632 pixels in total; gullied and non-gullied HiRISE-identified slopes: 1,648 pixels in total) to account for the influence and biases of the general pre-existing topography, resulting in normalized data. Densities for all gullies (2) and active gullies (4) were calculated by (2) dividing the number of all gullies by the total area with gullies based on CTX imagery (in pixels) for each orientation, and (4) dividing the number

291 of all active gullies by the total area with gullies based on multi-temporal HiRISE imagery (in
292 pixels) for each orientation, respectively.

293

294 **2.2.5. Slow small-scale displacement detection**

295 To investigate the possibility of small-scale movements like creep as precursors to gully activity,
296 which can only be observed over multi-annual time scales, we applied a method called digital
297 image correlation (DIC). We produced four HiRISE-DTMs of region 11 to investigate the flow
298 event that occurred between MY32 and 33 (Figure 4) as well as to study general gully activity in
299 the region. We used five HiRISE-images: PSP_005621_1090, ESP_023290_1090,
300 ESP_030859_1090, ESP_039747_1090 and ESP_048608_1090 to cover the time between MY 28
301 and 33. DTM production was conducted using the Ames Stereo Pipeline (ASP, Beyer et al., 2018).
302 Governed by the available HiRISE images, all produced DTMs are either pre-event or co-event
303 DTMs, i.e., no post-event DTM could be produced. The change in surface appearance and texture
304 due to the recent flow feature that occurred between MY 32 and 33 is minimal and did not influence
305 the quality of the image matching during stereo correlation. All images were bundle adjusted and
306 matching was performed with a Bayes EM-weighted affine adaptive window correlator to ensure
307 the highest possible DTM quality. Due to the good correlation quality, the point cloud files could
308 be meshed to DTMs with very high spatial resolutions ranging from 0.5 to 3 m/pixel. Despite the
309 low noise content, all DTMs feature distinct striped inter-CCD seam artifacts that are common for
310 HiRISE-based DTMs. Tab. 2 in the Appendix reports additional relevant details about the
311 produced and used DTMs.

312 Orthorectification was performed using the Ames Stereo Pipeline, where DTMs from timeframes
313 MY 28 to 30 and MY 28 to 33 have been used to orthorectify HiRISE images PSP_005621_1090,

314 ESP_023290_1090, and ESP_048608_1090 (Figure 10). This was necessary because digital image
315 correlation (DIC) needs highly accurate orthorectification to extract small-scale horizontal surface
316 displacements.

317 DIC is an image processing technique that allows for the quantification of coherent, in-CVP
318 (camera viewing plane) surface displacements in multi-temporal imagery (Ayoub et al., 2009;
319 Heid and Kääb, 2012; Bickel et al., 2018). The technique is limited by its ability to co-register
320 pixel neighborhoods within a specified search window, i.e., incoherent or too large surface
321 displacements between two image acquisitions will cause a loss of signal. This usually limits the
322 applicability of DIC to monitoring of continuous and slow displacements, e.g., of glaciers (Heid
323 and Kääb, 2012), volcanic edifices (Casu et al., 2011), and slow moving landslides (Bickel et al.,
324 2018). This limitation is particularly restrictive for space- and airborne sensors, as revisit rates are
325 usually lower and the displacement of objects between two acquisitions might be larger, and
326 potentially, too large. On Mars, DIC has successfully been applied to monitor dune migration and
327 sand fluxes using HiRISE imagery, e.g., in Nili Patera (Bridges et al., 2012) although it was
328 unsuccessful for coseismic displacement of faults in Cerberus Fossae on Mars (Grindrod et al.,
329 2018).

330 The three above mentioned orthorectified HiRISE images have been selected for the DIC analysis
331 for two reasons: 1) Their maximum temporal baseline, as a larger difference in time will allow for
332 the detection of smaller displacements (PSP_005621_1090 of MY 28 and ESP_048608_1090 of
333 MY 33); and 2) As they could potentially indicate pre-event displacement in the gully of interest
334 (PSP_005621_1090 of MY 28 and ESP_023290_1090 of MY 30). Prior to DIC ingestion, a
335 dynamic contrast enhancement has been applied (Wallis filter) and all orthorectified images were
336 co-registered with sub-pixel accuracy, as past studies have found that these steps generally increase

337 the correlation quality and coverage of the displacement field, if present (Bickel et al., 2018).
338 Subsequently, a frequency domain-based DIC code that is applying a Fast-Fourier-Transform
339 (Bickel et al., 2018) has been used to analyze the potential displacement between both image pairs,
340 using varying template and search window sizes. No post-processing of the results has been
341 performed to maintain the full interpretability of the results.

342

343 **2.2.6. Thermal investigations and seasonal frost coverage**

344 For thermal investigations, we collected all TES surface temperature datasets from MY 24 to 26
345 (except some measurements in MY 25 due to the influence of a global dust storm, see above) and
346 binned them into five groups of 2° of latitude from 66° to 76° . We then calculated the mean of all
347 individual measurements at the same time with their associated standard deviation (black lines of
348 red dots in Figure 11). For our thermal studies, we investigated all available surface temperature
349 datasets of all years together (except some data from MY 25 due to a global dust storm). No further
350 division into different MYs was done because annually variations of MY 24 and 26 are small and
351 negligible.

352 Furthermore, we also detected and investigated the seasonal frost coverage based on CTX and
353 HRSC imagery. We identified seasonal frost coverage by its bright appearance compared to
354 unfrosted regions (well-defined during the sublimation phases in spring by dark defrosting spots)
355 and the assumption, that the study region is covered by surface frost during the winter, which was
356 shown by Raack et al. (2015) in the same study region and substantiated by the general low surface
357 temperatures during winter (Piqueux et al., 2003). For investigations of the timings of surface frost,
358 we looked into all available CTX and HRSC images of the study region. We generalized the frost
359 cover and marked an image as “frosted” even when only a small part of the image shows bright

360 ice cover. This results in detailed information on the timing of surface frost in the complete study
361 region based on two different datasets without detailed analyses of local differences of frost
362 coverage such as orientations and altitude.

363

364 **3. Results**

365 We have identified 25 regions with multi-temporal HiRISE coverage (see black rectangles in
366 Figure 2), 13 regions include coverage of gullies. In total, 2,067 individual gullies were identified
367 on multi-temporal HiRISE images. In seven regions we identified contemporary active mass
368 wasting features within gullies. Overall, we found only 35 (~1.7 %) individual gullies that showed
369 activity within MY 28 to 34 (yellow dots in Figure 2 and Supplementary Table 01). One large
370 gully showed two independent activities at two different places in the wide alcove, therefore we
371 classified these activities as gully independent activities 32 and 33 (see Supplementary Table 01).
372 The activity can be divided into flow-like features ($n = 22$), as well as block movements within
373 gullies ($n = 16$), where three of them are combined features which makes 35 active gullies in total.
374 For seasonal investigations, multi-temporal coverage of some images within one martian year are
375 necessary. Due to the greater frequency of HiRISE-coverage of some regions within the study
376 area, we were able to narrow-down the activity of 10 gullies during one martian year.

377

378 **3.1. Present-day mass wasting activity on multi-temporal HiRISE imagery**

379 Present-day activity was defined by clearly visible erosion and/or deposition of material down a
380 gully. Although some gullies could also show seasonally generated albedo differences and dark
381 flow-like features, no sediment transport was detectable in these gullies so we classify these gullies

382 as “non-active”. We distinguished between flow-like features (dark toned flow-like forms with
383 visible transport of material) and block movements (movement of blocks down the gully slope).

384

385 **3.1.1. Flow-like features**

386 The most widespread present-day activity of gullies are flow-like features. We found 22 gullies
387 with active flow-like features or new deposits and erosion forms most likely caused by flow-like
388 activity. Three of them are associated with identifiable block movements. Ten of these 22 active
389 gullies show flow-like activity within only one MY and six of these ten gullies show repeated
390 activity. In detail, three gullies show activity in two separate MYs, two gullies within three
391 different MYs, and one gully shows activity within five MYs (see Supplementary Table 01).
392 Movements within repeatedly active gullies originated in the same places and covered the same
393 depositional areas of the gully.

394 Flow-like features have identifiable transport of sediment, which is probably dust and/or sand
395 (Raack et al., 2015). The presence of pervasive surface sand/dust is supported by the presence of
396 pervasive surface ripples and the seasonal appearance of dark spots on gully aprons, and next to
397 or within gully channels. These dark spots are likely formed by transport of sand and dust from
398 under the translucent slab ice (e.g., Piqueux et al., 2003; Kieffer et al., 2006; Thomas et al. 2011)
399 as larger particles cannot be mobilized (see further discussion of these features in Section 4.1).

400 Based on our seasonal observations, we found that the flow-like features occurred episodically,
401 i.e., changes appeared between two images and were not gradual. This was observed as an
402 accumulation of gully channel material in the "before" image, whereas the "after" image displayed
403 distinct flow features over the apron (Figure 3). Sometimes, the deposited material was observed
404 without observable accumulation of material in the channel beforehand. The flow-like features

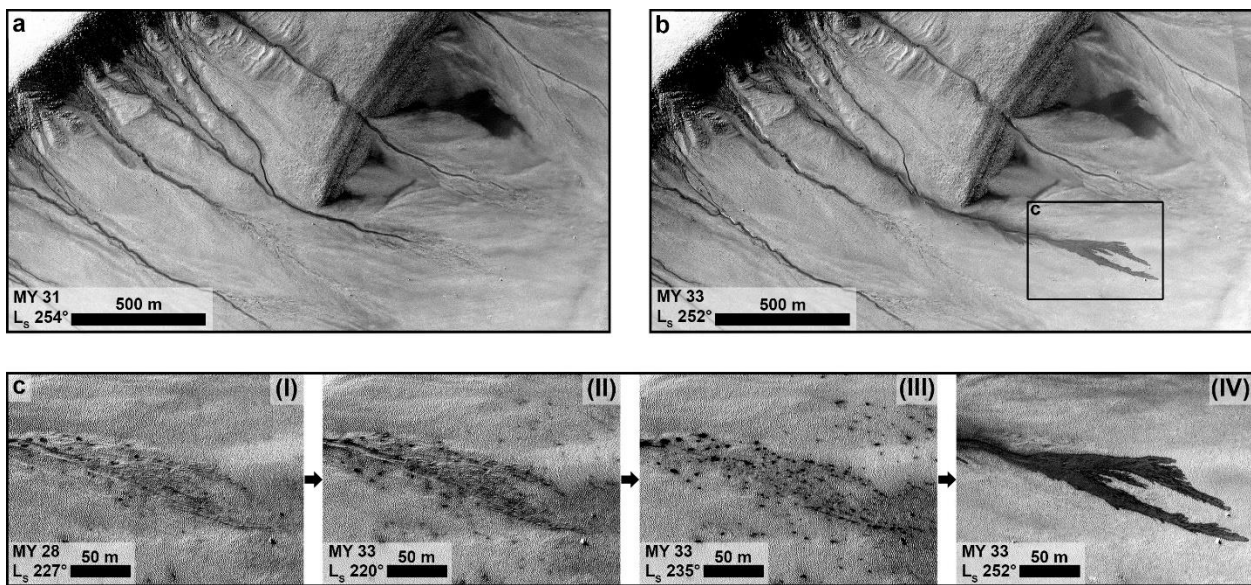
405 appear dark compared to their surroundings. Over time, the transported material brightens and
406 fades until mid-summer, which could be due to gradual deposition of dust, comparable to the
407 fading of, e.g., dust devil tracks (Reiss et al., 2016) and slope streaks (Schorghofer et al.,
408 2007). However, fading of a flow-like feature in Sisyphi Cavi was also observed by Raack et al.
409 (2015) and their investigation of the corrected Lambert albedo images showed that the flow-like
410 feature did not brighten, but that the surroundings darkened over time due to seasonal frost
411 sublimation. In summer, the surroundings and the flow-like features have a very similar albedo
412 which can only be observed in the corrected albedo images. This indicates that the brightening is
413 not caused by dust deposition but is a result of frost sublimation. The brightening did not appear
414 to alter the changes in surface relief associated with the dark flow-like features, therefore this study
415 will focus on the formation of these mass movements and not their fading.

416 In some cases, seasonal observations were not possible and no dark flow-like features were
417 identifiable, but a change of the surface relief caused by sediment transport was still visible. In
418 Figure 4 an example flow-like feature is shown, with the formation of relatively small new
419 transportation channels (Figure 4b), block movement (Figure 4b), erosion of ripples or
420 superposition of ripples with transported material (Figure 4c), and a general change of the relief of
421 the surface. Thickness and consequently volume calculations cannot be made because it was not
422 possible to measure the height of the newly formed deposits, either on digital terrain models
423 (DTMs) or with shadow measurements (for some volume estimations, see Raack et al., 2015). This
424 indicates that the deposits have a thickness of some decimeters or less.

425 One gully (#3) in the study region had clearly identifiable headwall erosion and loss of material,
426 which was transported down the gully. This was the only gully where the source region of
427 transported material was clearly visible and measurable (Figure 5). Raack et al. (2015) analyzed

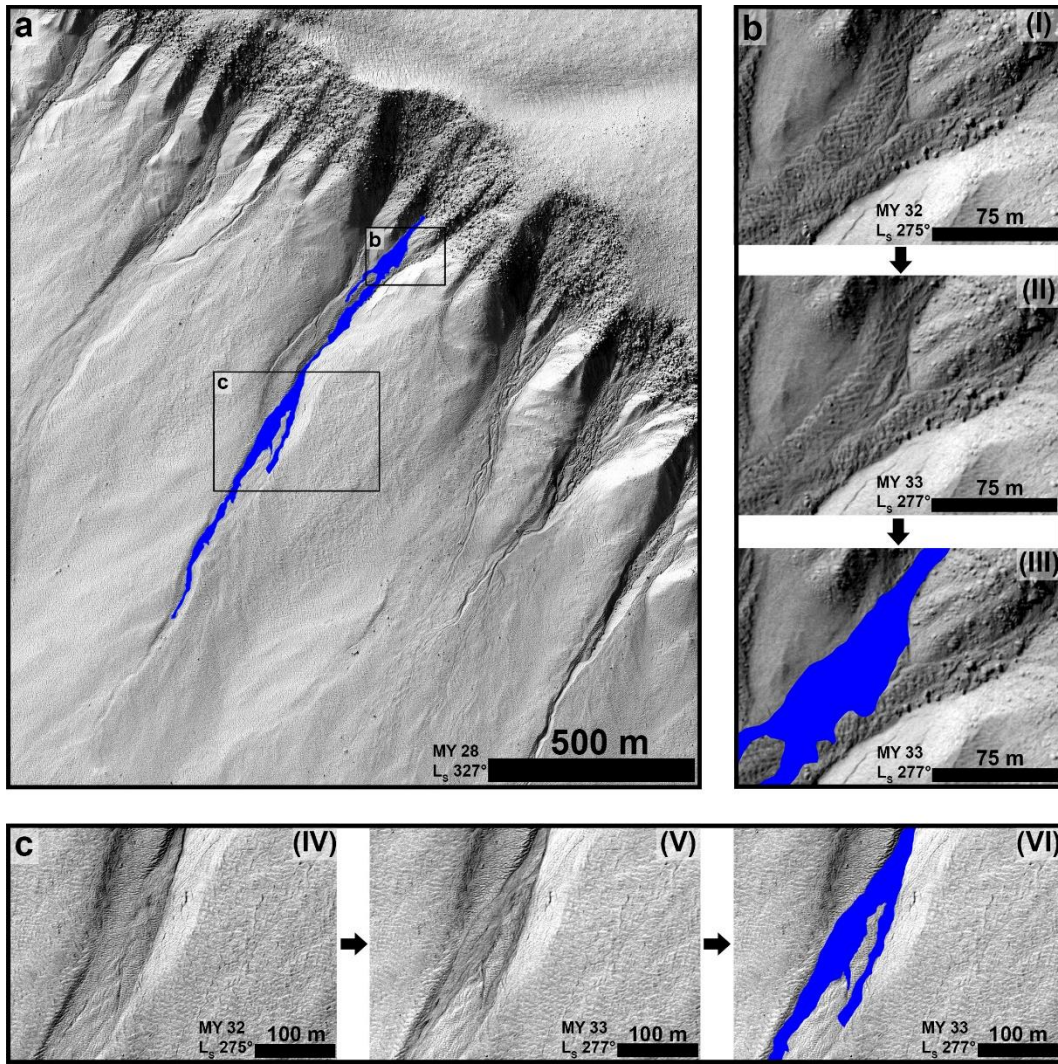
428 the same gully but no source region for the identified activity was found as it only became apparent
429 in more recently acquired images. At some localities, the gully-alcove headwall erosion of up to
430 several meters (max. ~5 m) occurred between MY 29 and MY 33. This headwall erosion is the
431 first and only evidence of a clearly identifiable source region for transported material in the study
432 region.

433 The only noticeable features located upslope of observed sediment transport are small (up to ~15
434 m), dark flow-like features on the steep flanks of the gully channels (Figure 6). These features
435 were found in some active gullies, as well as in non-active gullies. We infer that sediment erosion
436 and transportation are taking place at these locations, because there dark layers paralleling the crest
437 of the gully channel flanks (Figure 6 d-e), from which the small dark flow-like features emanate.
438 A second indicator for sediment transport, even if it is not topographically visible, is the
439 accumulation of dark material within gully channels (Figure 6). These accumulations are formed
440 by confluence of the small, dark flow-like features. This was also proposed, but not directly
441 observed by Raack et al. (2015), due to the lack of datasets with sufficiently high resolution.



442

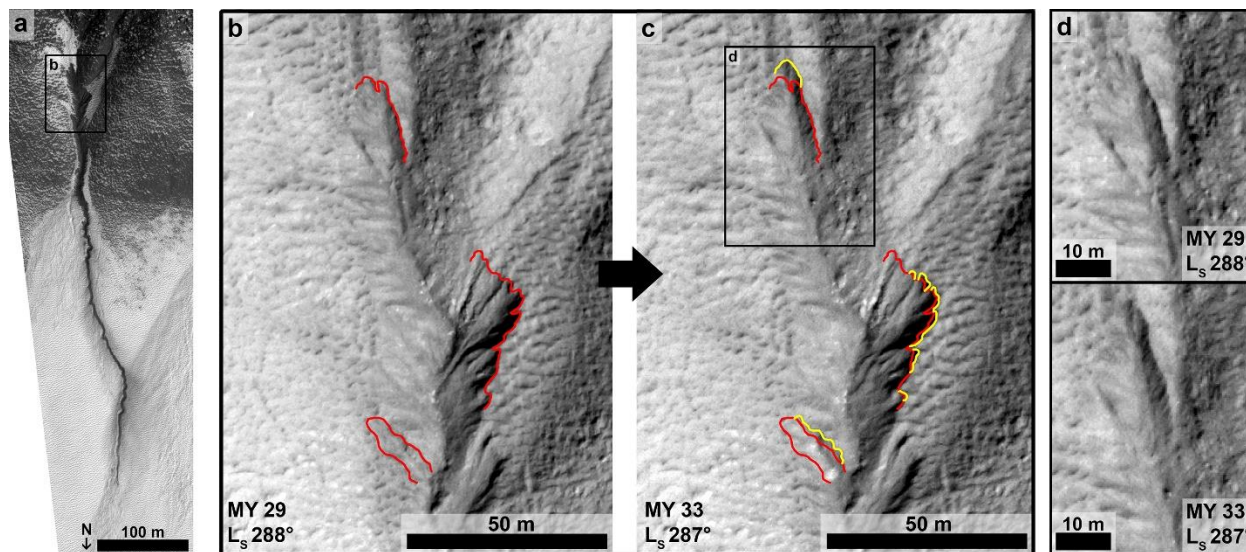
443 **Figure 3:** Before and after images of a south-east facing slope of a polar pit (Region 5, see Figure
444 1) within MYs 31 and 33 at comparable L_s of 254° **(a)** and 252° **(b)**. The downslope direction is
445 from top left to bottom right. The active part of the gully in the middle of the images (gully #1,
446 same as gully N in Figure 8b) is apparent because of the appearance of a dark flow-like feature in
447 MY 33, which superposes the existing apron and has deposited new material. **(c)** I-IV Detailed
448 views of the evolution of the appearance of the active part of the apron in MY 28 (L_s 227°) and
449 MY 33 at L_s 220° , 235° , and 252° . Between the first (*I*, MY 28) and the second image (*II*, MY 33
450 at L_s 220°), there is no identifiable change of the surface, except for in the pattern of the annually
451 active dark defrosting spots. Between the second (*II*) and the third (*III*) image, these dark defrosting
452 spots expand, but no flow is visible. 26 sols later in the fourth (*IV*) image, a dark flow is visible
453 and the dark defrosting spots are no longer visible, which indicates advanced sublimation of the
454 slab ice and probably the complete defrosting of the surface. HiRISE-images **(a)**
455 ESP_030503_1115, **(b)** ESP_048107_1115, **(c)** (*I*) PSP_003511_1115, (*II*) ESP_047039_1115,
456 (*III*) ESP_047751_1115, (*IV*) ESP_048107_1115. North is up in all images.



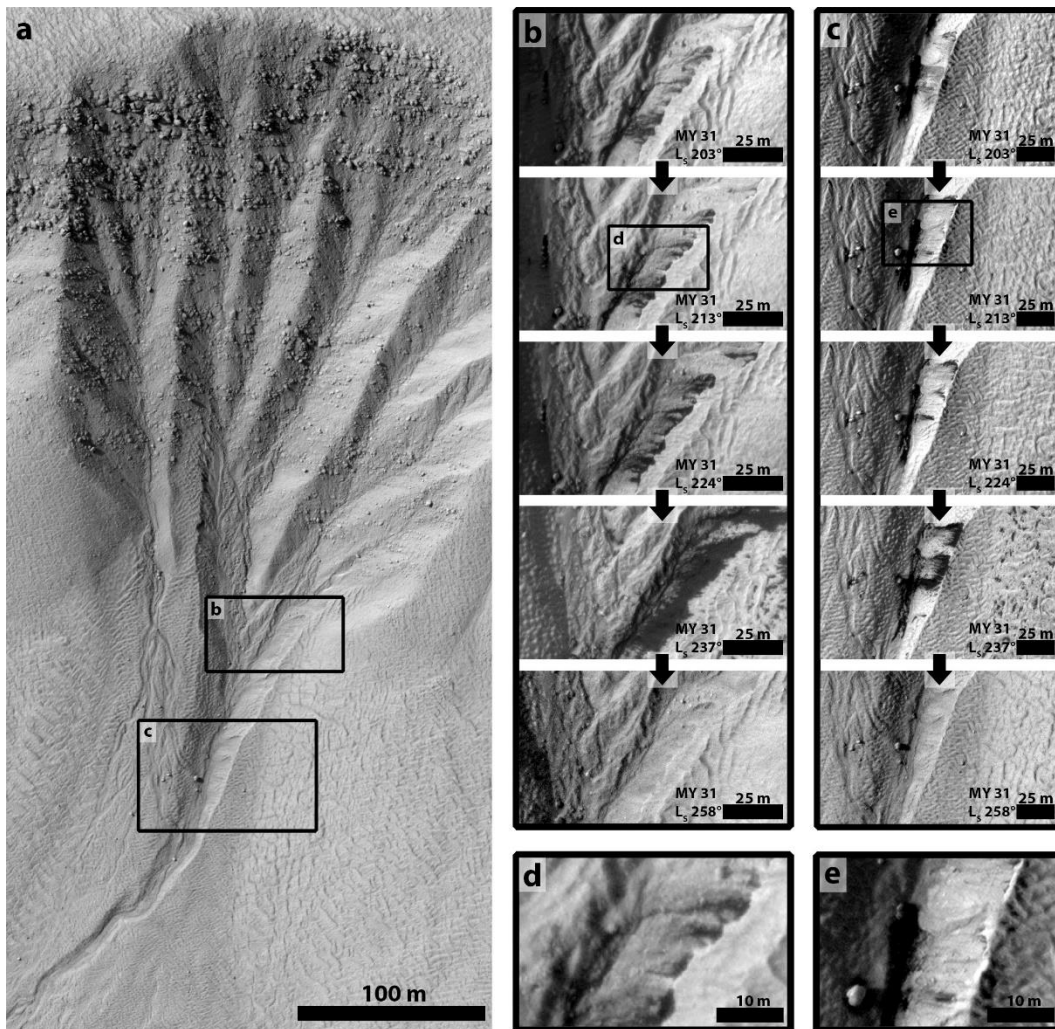
457

458 **Figure 4:** (a) Present-day active gully #11 (MY 28, L_s 327°) on a south-west facing slope in
 459 Region 11 (see Figure 1 and gully A of Figure 8a). The area within the gully affected by the activity
 460 (erosion and deposition of material) is mapped in blue. With more than 1 km in length, this active
 461 mass wasting form was the largest identified in this study. (b) (I-III) Close-ups of a part of the
 462 gully alcove before (I), in MY 32 at L_s 275°, and after (II), in MY 33 at L_s 277°, almost exactly
 463 one martian year apart. The third image (III) shows the affected region (mostly by erosion) mapped
 464 in blue. (c) (IV-VI) Close-ups of a part of the gully's transportation channel before (IV), in MY 32
 465 at L_s 275°, and after (V), in MY 33 at L_s 277°, comparable to (b) in terms of timing. Similarly, the
 466 third image (VI) shows (mapped in blue) the region affected by activity, by erosion, as well as

467 deposition. HiRISE-images (a) PSP_005621_1090, (b) (I) ESP_039747_1090, (II and III)
 468 ESP_048608_1090 (c) (IV) ESP_039747_1090, (V and VI) ESP_048608_1090. North is up in all
 469 images.



470
 471 **Figure 5:** Headwall erosion of active gully #3 presented in Raack et al. (2015) (also seen in Figure
 472 8b – gully G). (a) Overview of the active gully. The gully shows activity every year in the form of
 473 a large, dark flow within the gully channel and new material superposition on top of the gully
 474 apron (Raack et al., 2015). (b) Detail of the gully alcove in MY 29 at the beginning of summer (L_s
 475 288°). The large gully alcove was filled with material (rippled surface, presumably ice-rich mantle,
 476 e.g., Mustard et al., 2001; Raack et al., 2012), which is eroded, leading to a smaller gully alcove.
 477 Red lines represent clearly identifiable outlines of the headwall of the alcove. (c) In MY 33 at the
 478 beginning of summer ($L_s 287^\circ$) headwall erosion of a few meters could be identified (yellow lines
 479 represent the new headwall of the alcove). Especially the uppermost region of the gully alcove
 480 shows the highest erosion rate within the four martian years. (d) Detail of the top of the gully
 481 alcove in MY 29 and 33. Erosion of a few meters of material is clearly visible. HiRISE-images (a)
 482 ESP_029725_1115, (b) ESP_013585_1115, and (c) ESP_048819_1115. North is down in all
 483 images as indicated.



484

485 **Figure 6:** (a) Example of a gully alcove with identifiable small, dark flow-like features emanating
 486 from a layer on gully channel flanks. Here, the small, dark flow-like features are too small to show
 487 any transported sediment. The small, flow-like features accumulate within the gully channel, but
 488 there is no associated large flow-like feature with transported material. (b) + (c) Two detailed
 489 image time series of the gully channel from beginning of spring (Ls 203°) until the end of spring
 490 (Ls 258°) where defrosting is at its maximum. Dark material flows down the gully channel flank
 491 into the interior of the channel. Here, dark material accumulates and flows down the gully channel,
 492 which is detectable in (c). (d) + (e) Details of the layer on the gully channel flanks from where the
 493 dark material emanates. The layer is only several meters wide and identification with HiRISE

494 images is difficult. **(a)** Overview: HiRISE-image ESP_040486_1105 (Ls 309°). **(b)** + **(c)**
495 Sequence: HiRISE-images ESP_029475_1105, ESP_029686_1105, ESP_029897_1105,
496 ESP_030174_1105, and ESP_030609_1105. North is up in all images.

497

498 **3.1.2. Activity of block movements**

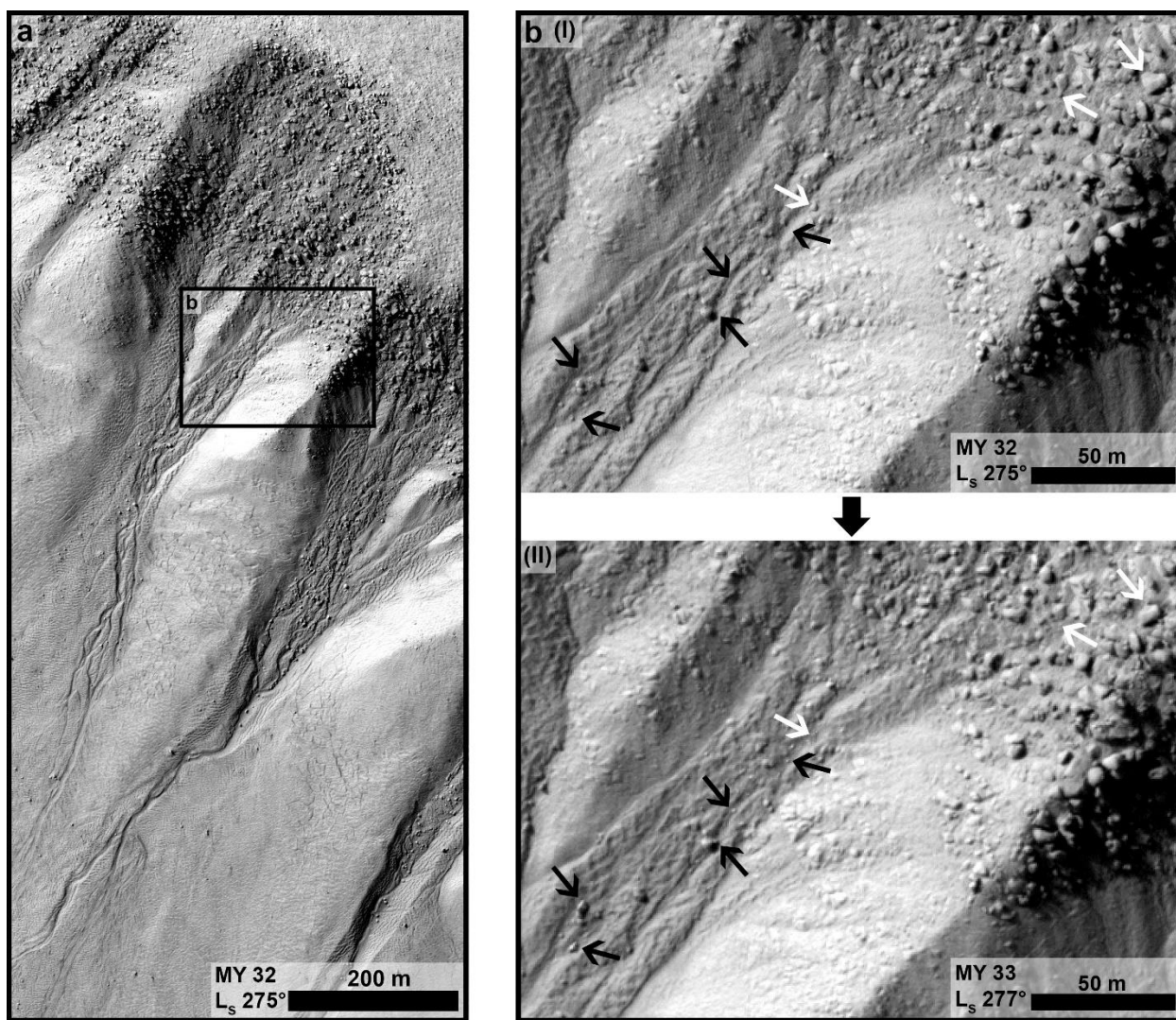
499 Block movements are clearly identified transported blocks of about 1-2 m in diameter between
500 images which could have slid, tumbled or rolled down slope under gravity or have been transported
501 in a flow. In the study region, block movements only occur within gully alcoves where slopes are
502 relatively steep and have undergone more recent modification compared to non-gullied slopes.
503 Furthermore, gully alcoves uncover an underlying rocky surface, which is otherwise superposed
504 by a mantling deposit in this region (Figure 7). This rocky surface is often the source for blocks,
505 which then move down the slope.

506 We observed 16 different gullies (three of them also associated with identified dark flow-like
507 features) with identifiable block movements within the study region. Only one block movement
508 could be seasonally investigated (Figure 12), while all other block movements occur in regions
509 with only limited temporal HiRISE-coverage. The number of 16 block movements is a minimum
510 number because block movements are hard to identify and some block movements (particularly
511 short displacements) are likely to have been missed during our investigations. Three of the
512 identified gullies show a combined activity of flow-like features and block movements. Here,
513 blocks moved several meters in the same direction as the flow-like features and/or were superposed
514 by transported material. In the last case it is hard to distinguish between moved blocks or just
515 superposed blocks by loose fine material. Tracks associated with the block movements were not

516 found. Only in one case (Figure 7), the path of the block down the slope is roughly traceable by
517 the displacement of some other blocks.

518 The distance moved by the blocks varied between ~1 m to 230 m at maximum (Figure 7b). Most
519 blocks moved only 1-2 meters (n = 9), which typically corresponds to a block rolling from one
520 face to another. The other remaining block movements (n = 6) moved between 5 and 40 meters.

521 In one case, a block seemed to disappear completely, which means it was not found in the ‘after’-
522 image and therefore the travel distance could not be measured.



523

524 **Figure 7: (a)** Gully #12 with present-day activity in form of block movement within the alcove in
525 Region 11 (see Figure 2) on a south-south-west facing slope. Overview image **(a)** and detail **(b)**
526 *(I)* were taken in MY 32 at L_s 275°. **(b)** Detail is presented as before *(I)* and after *(II)* images
527 whereupon the after *(II)* image was taken nearly exactly one martian year later (MY 33 at L_s 277°)
528 than the before image. White arrows point to eroded/disappeared blocks, while the black arrows
529 point to newly deposited blocks. The transported blocks are generally only a few pixels in diameter
530 (~1 m); only the largest block (lower left) has a diameter of about 4-5 m. HiRISE-images **(a)** and
531 **(b)** *(I)* ESP_039747_1090, **(b)** *(II)* ESP_048608_1090. North is up in all images.

532

533 **3.2. Topography, orientation, and digital image correlation**

534 To identify possible mechanisms responsible for the identified present-day activity of gullies in
535 Sisyphi Cavi, we investigated the topography of the active gullies based on HiRISE DTMs, the
536 orientation of all slopes and gullies in the study region, and possible small-scale surface changes /
537 activities based on digital image correlation of HiRISE images.

538

539 **3.2.1. Topography**

540 We measured the topographic long profiles of selected gullies on slopes of region 11 (Figure 8a)
541 and region 5 (Figure 8b) by tracing the path of the gullies from the top of the alcove to the end of
542 the depositional fan. Gullies marked by red profiles in Figure 8 show present-day activity and the
543 position of the activity is bracketed by black bars with arrows.

544 In region 11, the shape of all the gullies (6 measured gullies, 3 with present-day activity) is very
545 comparable (Figure 8a (1)), and no systematic differences in the general shape of the long profile
546 between active and non-active gullies could be identified. All gullies have a rectilinear profile with

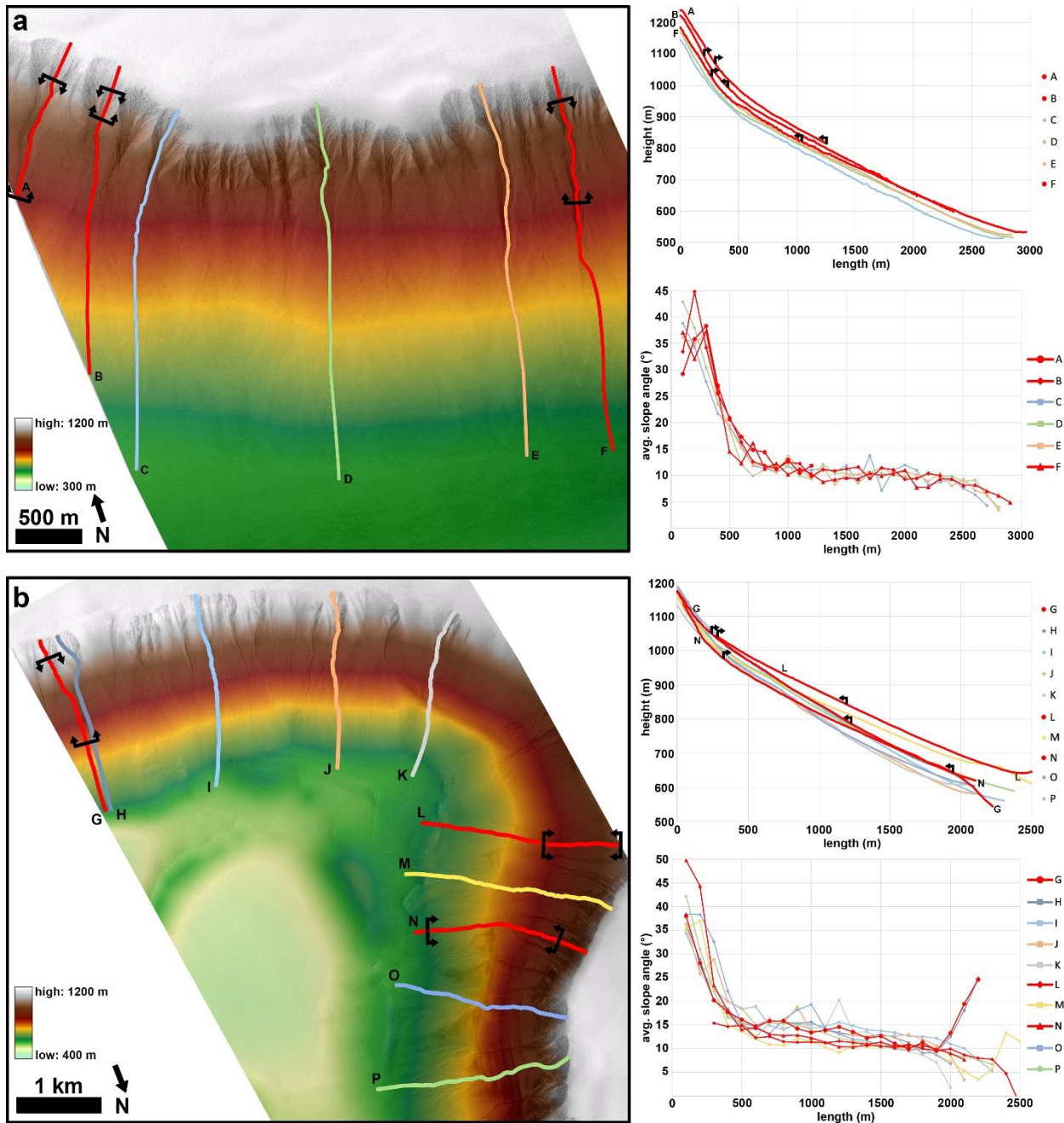
547 a steeper upper part and shallower lower part, which starts around 400 m downslope,
548 corresponding to the change from exposed rocks to fans. Present-day activity originates at the
549 steeper upper part of the gullies and material is subsequently transported down the gully channel
550 to where slopes are shallower (around 10°-15°).

551 Furthermore, the average slope angles calculated every 100 meters of gully length (Figure 8a (2))
552 are broadly similar. The average slope angles in the alcove area reach maxima of between 30° and
553 45° and diminish to around 20° towards the base of the alcoves. The alcoves show a higher
554 variation in slopes compared to the rest of the profiles. The remaining downslope parts of the
555 profiles have relatively constant slopes of around 10°, which drop to 5° in the last few hundred
556 meters. Two of the three active gullies (A and B) have steeper average slope angles in the first 200
557 to 300 m, while other non-active gullies only show shallower slope angles. Gully slopes A and B
558 could be not measured in their entirety (the end of the profile is missing) because the DTM does
559 not cover the complete slope.

560 The profiles of the gullies in region 5 are very comparable to those in region 11. However, they
561 appear a somewhat smoother and have shorter, steeper upper parts (around 200-250 m) than the
562 gullies in region 11 (Figure 8b (3)). Comparable to region 11, gully activity originates on the
563 steeper slopes at the beginning of the gully profile and continues down to shallower sloping
564 regions. Furthermore, the gullies in region 5 are also very comparable to each other, except gully
565 L, which appears smoother at the beginning than the others and has a steeper slope angle at the
566 end (similar to gullies H and M). The smooth beginning is because the top of the profile is not
567 included in the DTM. The increase of average slope angles at the end is caused by the occurrence
568 of a ridge at the base of the slope (Figure 8b (4)). All other profiles show comparable patterns as
569 well as comparable average slope angles. Slope angles decrease from up to ~50° (alcove of gully

570 N) down to $\sim 0^\circ$ (apron of gully L). Consequently, no differences of active and non-active gullies
571 in region 5 was found.

572 The average slope angles of all measured gullies of both regions are provided in Supplementary
573 Table 02. The average slope angles for the entire lengths of all measured gullies varied between
574 16° and 10° (gullies A and B are not taken into account because the profiles do not extend to the
575 terminus of the hillslope and therefore have anomalously higher average slope angles). The
576 average slope angles of for the entire lengths of the active gullies ranges between 15° and 10° ,
577 which provides additional confirmation that no difference in topography between active and non-
578 active gullies is measurable.



579

580 **Figure 8:** (a) Colorized DTM from HiRISE stereo pair ESP_023290_1090 and
 581 ESP_048608_1090 in region 11 (see Figure 2) with semi-transparent orthophoto. On the right side
 582 are the associated topographic profiles as a function of height vs. distance from top of the alcove
 583 (above) and as a function of average slope angles as calculated over 100 m segments (see also
 584 table 1) vs. distance (below). The profiles start at the crest of the alcove and end at the visually

585 identified terminus of the hillslope. Note that the termini of measured gullies (aprons) often stop
586 before the end of the slope. Active gullies (A, B, and F) are marked in red; between the areas of
587 the black bars with arrows, contemporary activity was identified. (b) Colorized DTM of HiRISE
588 stereo pairs ESP_013097_1115 and ESP_013585_1115 in region 5 (see Figure 2) with semi-
589 transparent orthophoto. See also Raack et al. (2015) for more information of this specific area. On
590 the right side same profiles as in (a). Active gullies (G, L, N) are also marked in red. Profiles G
591 and H have increasing slopes at the end of the profile due to the presence of a small local
592 depression. However, this has no influence on the gullies because the depression is located beyond
593 the end of the gully deposits.

594

595 **3.2.2. Orientation**

596 To identify a possible triggering mechanism of gully activity and to find differences between active
597 and non-active gullies, the orientations of gullies, gully densities, and gullied slopes based on CTX
598 and HiRISE imagery of the complete study region were investigated. Four different measurements
599 were performed:

600 (1) Orientation of pixels identified on MOLA gridded data (460 m/pix) of gullied slopes
601 (slope angle $> 6^\circ$) found on CTX imagery. In total, 8,303 pixels cover all gullied slopes
602 and show a clear north-south trend (Figure 9a). After normalization against all slopes
603 $> 6^\circ$ in the complete study region (35,329 pixels), the north-south trend is still visible
604 (Figure 9b), but not so distinct compared to non-normalized data. Both the normalized
605 and non-normalized orientation plots show a slightly preferred south-facing (or pole-
606 facing) trend for all gullied slopes.

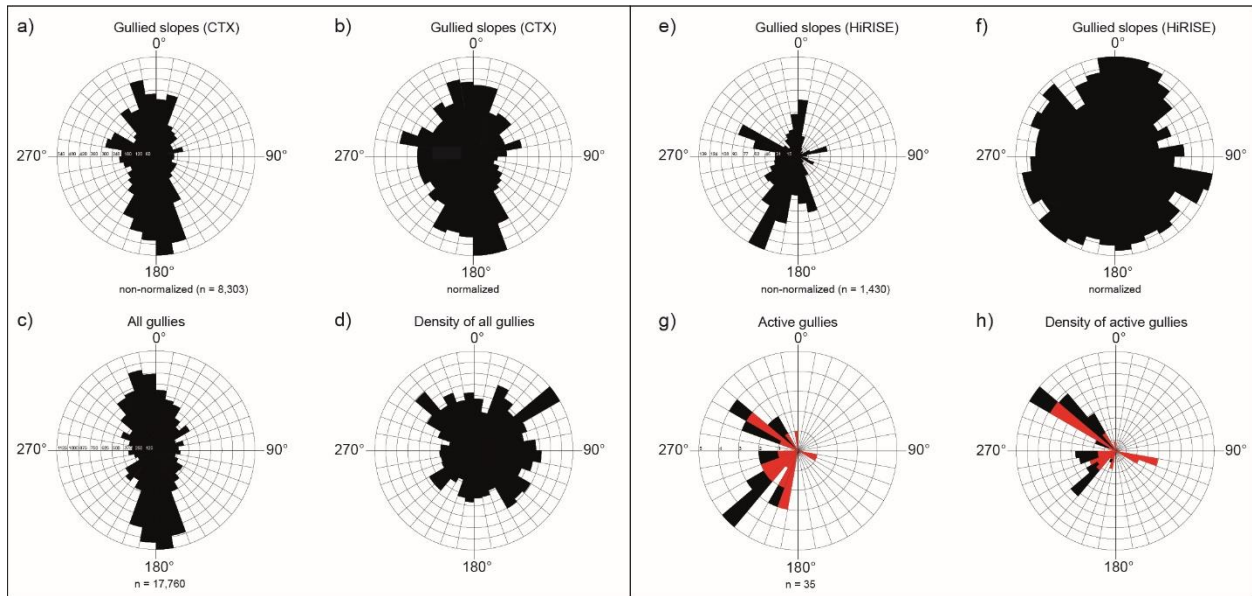
607 (2) Orientation of all gullies in the study region based on CTX imagery. In total, 17,760
608 individual gullies were identified and measured. The data show a strong north-south
609 trend with slightly more south-facing gullies than north-facing gullies (Figure 9c). The
610 density of gullies is remarkably uniform with orientation (Figure 9d). The highest peak
611 of gully density is found between 50° and 60° (northeast) and a slightly lower density
612 of gullies is found on south- to west-facing slopes.

613 (3) Orientation of pixels identified on MOLA gridded data (460 m/pix) of gullied slopes
614 (slope angle > 6°) found on multitemporal HiRISE imagery. In total, 1,430 pixels cover
615 all gullied slopes (Figure 9e), while only 218 pixels cover non-gullied slopes. This is
616 an effect of the intensive monitoring of gullied slopes with the HiRISE camera in this
617 region. After normalization against all slopes > 6° of multitemporal HiRISE-covered
618 slopes (1,648 pixels), a very uniform distribution is visible (Figure 9f).

619 (4) Orientation of all active gullies based on multi-temporal HiRISE imagery. In total, 35
620 individual gullies show present-day activity and were measured. The data show a
621 southwest and a northwest facing trend (Figure 9g). The color-coding represents dark
622 flow-like features (in red) and block movements (black). Only two gullies are east
623 facing. The density clearly shows a higher density of active gullies facing northwest
624 (Figure 9h). Same color-coding as in Figure 9g), which shows the highest density of
625 flow-like features orientated towards north-west. Comparison with Figure 9e reveals
626 that the lack of active east-facing gullies could be due to imaging bias, but that the lack
627 of north-facing active gullies is most likely real.

628 In summary, gullies tend to be oriented north-south in the study region with a slight bias towards
629 south-facing slopes and the highest density towards the north. In contrast, active gullies tend to be

630 oriented towards the northwest and to a lesser extent the southwest, with a lack of north-south
631 facing active gullies.



632
633 **Figure 9:** (a) Orientations of all sloping pixels with gullies based on MOLA data (n = 8,303) and
634 (b) the same data normalized against all sloping pixels. (c) Orientations of all mapped individual
635 gullies (n = 17,760) based on CTX imagery and (d) densities of all mapped gullies measured in
636 units of gullies per MOLA pixel (the data in c divided by a). (e) Orientations of all pixels with
637 gullied slopes included in multi-temporal HiRISE imagery (n = 1,430) and (f) normalized by the
638 total number of sloping pixels covered by multi-temporal HiRISE images. (g) Orientations of all
639 investigated present-day active gullies (n = 35) identified in multi-temporal HiRISE imagery (red
640 = dark flow-like features and black = block movements), and (h) densities of all active gullies
641 measured in numbers of gullies per pixel (the data in g divided by f), same color-coding as in (g).

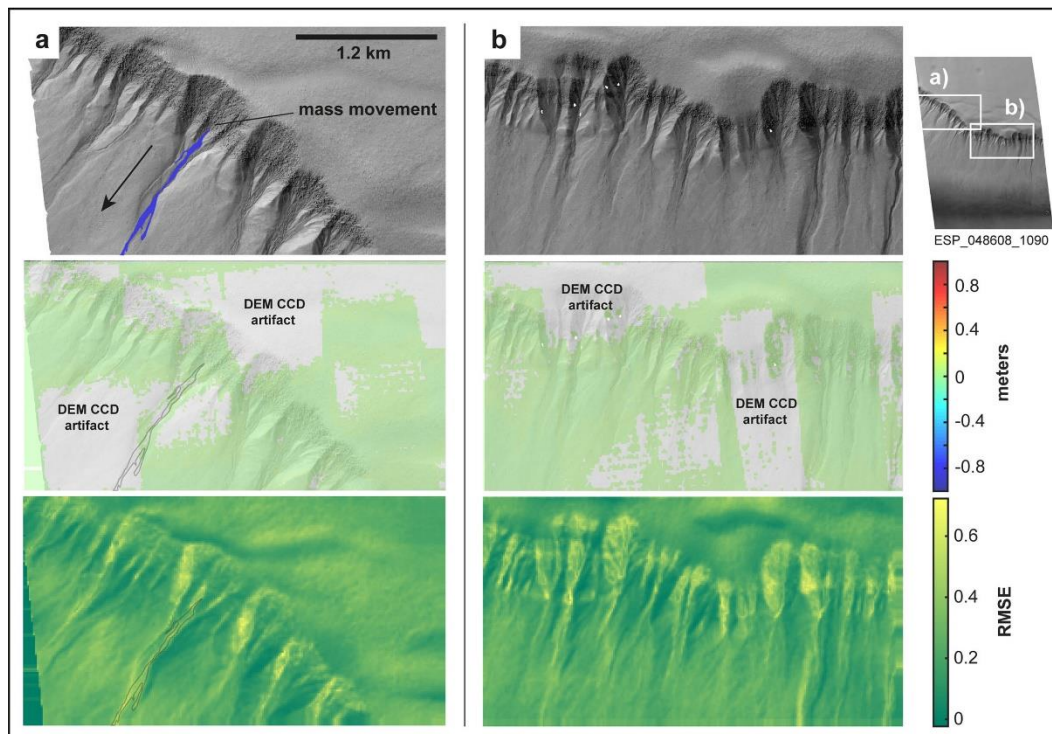
642

643 3.2.3. Digital image correlation

644 The correlation of both HiRISE pairs at location 11 that cover the event between MY32 and 33
645 (see also Figure 4) does not show any displacements in the periods from MY 28 to 30 (pre-event)

646 and to 33 (co-event), respectively (Figure 10). This could indicate that 1) there is no pre-event
647 displacement of the hillslopes hosting the investigated martian flow-like features, and 2) that there
648 is no slope creep occurring at all or that such creep is smaller than 25 cm within the five observed
649 martian years, i.e., less than ~5 cm per MY on average.

650 Parts of the displacement fields (Figure 10) show systematic and erroneous displacement values
651 that are the result of either 1) moving shadows that are caused by slightly different illumination
652 conditions for the used images or 2) inter-CCD seam artifacts. These types of artifacts cannot be
653 avoided, which is why the respective areas have been masked to maintain clarity (Figure 10). The
654 low root mean square error (RMSE) values, which are a measure for the quality of the image
655 correlation, across these affected regions of the images indicate that the rectangular patches in the
656 displacement fields are in fact caused by errors in the DTM used for the HiRISE image
657 orthorectification and are not actual (rapid) displacement.



658

659 **Figure 10:** Displacement magnitude and associated correlation RMSE between HiRISE images
660 PSP_005621_1090 and ESP_048608_1090 (MY 28 to 33, i.e., the image pair with the maximum
661 temporal baseline) with focus on two different sites along the cliff of interest in region 11: **a)** the
662 portion where activity occurred in MY 33 at $L_S 277^\circ$ (blue polygon, in the indicated direction)
663 (Figure 4), and **b)** a series of gullies further east. Images have been taken before (MY 28) and after
664 (MY 33) the activity of the gully. The accumulated displacement of the slope between MY 28 and
665 33 appears to be less than one pixel (~ 25 cm) or non-existent. Due to the occurrence of the flow
666 and due to systematic noise introduced by CCD artifacts, coverage of the region of interest is
667 incomplete. The correlation RMSE maps indicate areas in the images where matching accuracy
668 has been slightly reduced, particularly in the shadowed portions of the gullies (western gully
669 flanks). Overview based on HiRISE image ESP_048608_1090.

670

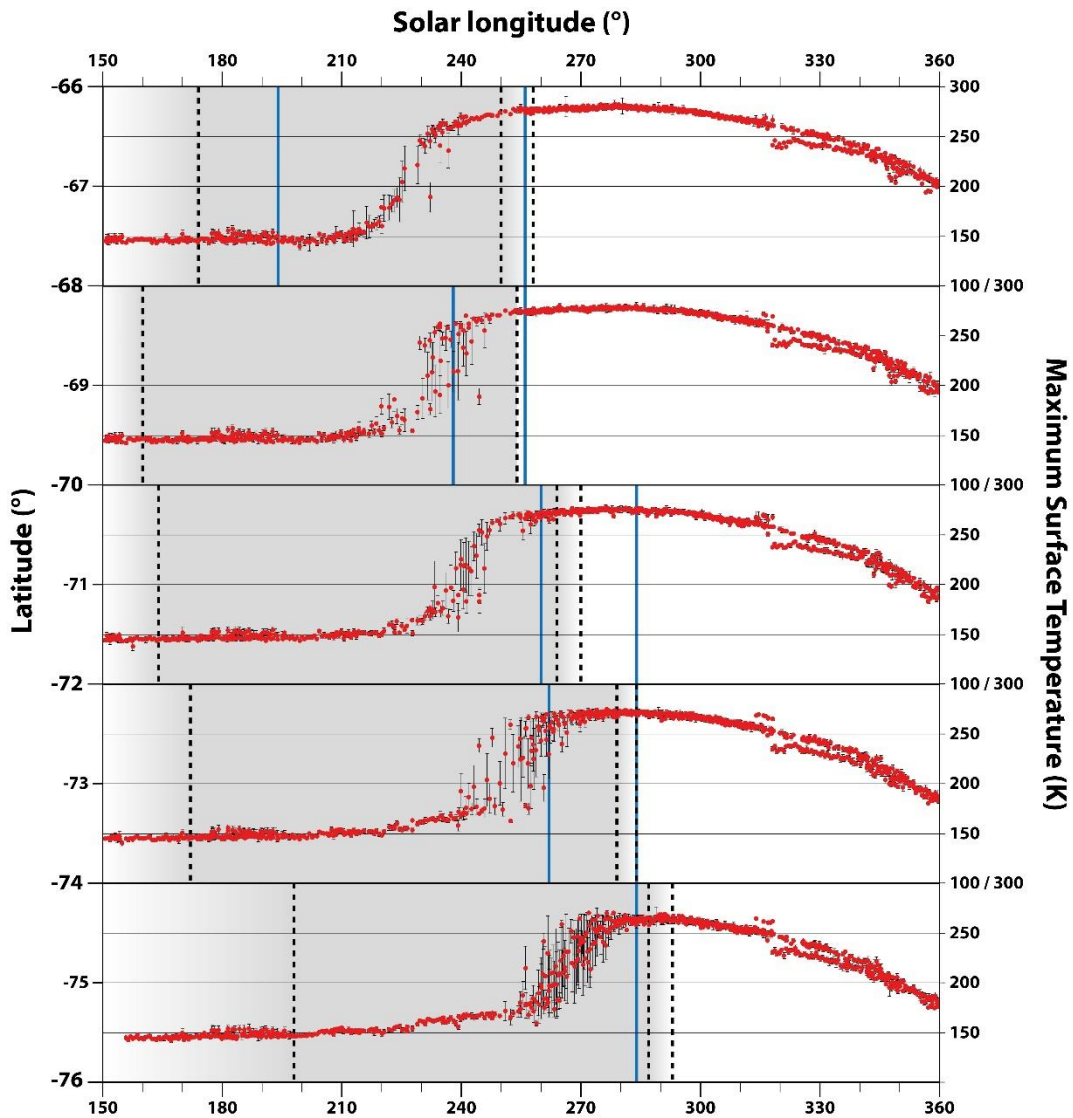
671 **3.3. Timing of annual surface ice cover and gully activity, surface temperatures, and** 672 **comparison to dark spots**

673 Based on our large dataset of CTX, HRSC, and HiRISE images, we were able to correlate seasonal
674 frost coverage with the annual activity of gullies. Using TES data we could correlate these trends
675 with surface temperature. According to Raack et al. (2015), this seasonal frost cover is composed
676 mainly of CO_2 ice with some minor contaminations of H_2O ice and dust. Figure 11 shows the
677 seasonal trend in surface temperature with latitude combined with our observations of visible
678 surface frost. Each latitude band has a similar temperature trend with temperatures stable at around
679 150 K until defrosting starts, the temperature then climbs relatively quickly and reaches a convex-
680 up plateau extending over the summer. For latitudes between 72 and 76° S there is a slight
681 precursor rise in surface temperature before the steep climb. The last image without surface frost

682 does not occur until $L_s \sim 30^\circ$ after the plateau is reached. For more equatorial latitudes the rise in
683 surface temperature is experienced earlier and is slightly more rapid with the surface frost
684 occurrence showing the same trend. At 75° S, the surface temperature plateau is reached at L_s
685 $\sim 280^\circ$, whereas at 67° S it is reached at $L_s \sim 240^\circ$.

686 Figure 12 shows the timing of the gully activity alongside observations of seasonal surface frost
687 cover from HiRISE. In almost all cases, the activity occurs at the very end of the surface defrosting.
688 The three exceptions are gully 3 in MY 29 and 31, and gully 7 in MY 31, where activity is earlier
689 in the year. These exceptions show the same type of activities compared to the others, but gully 3
690 is the only active gully in the study region orientated due north, which implies an earlier, more
691 intense sun exposure and earlier defrosting. This is the likely explanation for the relatively early
692 activity compared to the other active gullies. The active gully was investigated by Raack et al.
693 (2015) and shows clear headwall erosion of material in the source region (Figure 5). Gully 7 shows
694 an early block movement in MY 31 and this was the only active block movement whose timing
695 could be constrained in time. All other block movements appear in regions where a high-resolution
696 multi-temporal coverage was not available (see Supplementary Table 01). Therefore, whether
697 block movements systematically occur before the flow-like features in the study region could
698 neither be excluded nor confirmed.

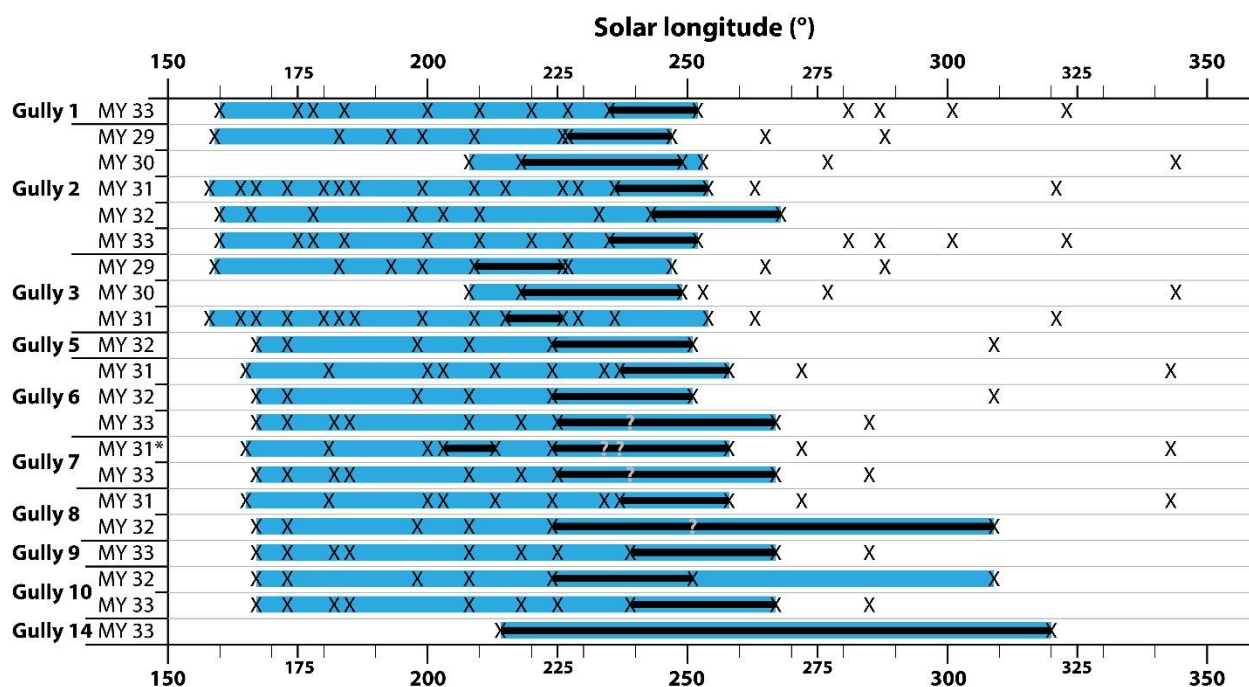
699 Seasonal frost coverage of the study region was easy to identify. During winter and early beginning
700 of spring, the surface appeared relatively bright and dark defrosting spots are visible mainly on
701 dunes. This bright appearance is probably caused by the redeposition of CO_2 frost on top of the
702 generally translucent slab ice cover. Later, while the defrosting process is occurring (mid to end
703 of spring), only small bright icy patches on the generally defrosted surface are clearly visible. Dark
704 defrosting spots appear on all dark dunes within the study region.



705

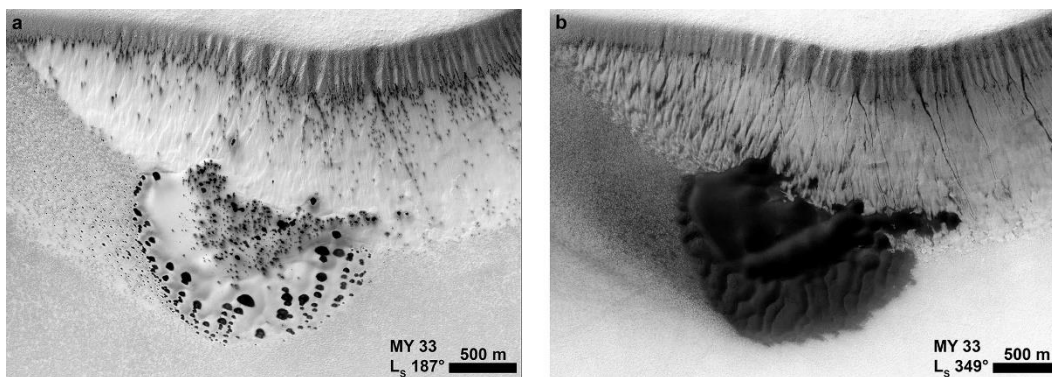
706 **Figure 11:** Schematic diagram of the average annual defrosting of the study region. Solar
 707 longitudes from end of winter (Ls 150° - 180°), spring (Ls 180° - 270°), to summer (Ls 270° -
 708 360°) of the southern hemisphere vs. latitude of the study region (left, subdivided into areas of 2°)
 709 and vs. maximum surface temperatures (right, TES) of the study region within subdivided regions.
 710 The grey bar within each subdivision represents the surface defrosting observed on CTX datasets
 711 of MY 28-34. The first dashed black line represents the timing of the first available image (frosted
 712 surfaces), the second dashed black line represents the timing of the last image with identifiable
 713 patches of surface frost, and the third and last dashed black line represents the timing of the first

714 image without any surface frost. The blue lines represent the timing of defrosting observed on
 715 HRSC imagery. The first blue line represents the timing of the last image with identified ice on
 716 the surface, the second line represents the timing of the first image without any surface frost. The
 717 red dots represent maximum daytime surface temperatures measured by TES of MY 24 to 26. The
 718 individual dots represent the average of all taken TES measurements at the same time (same solar
 719 longitude) with standard deviation (thin black “error” lines).

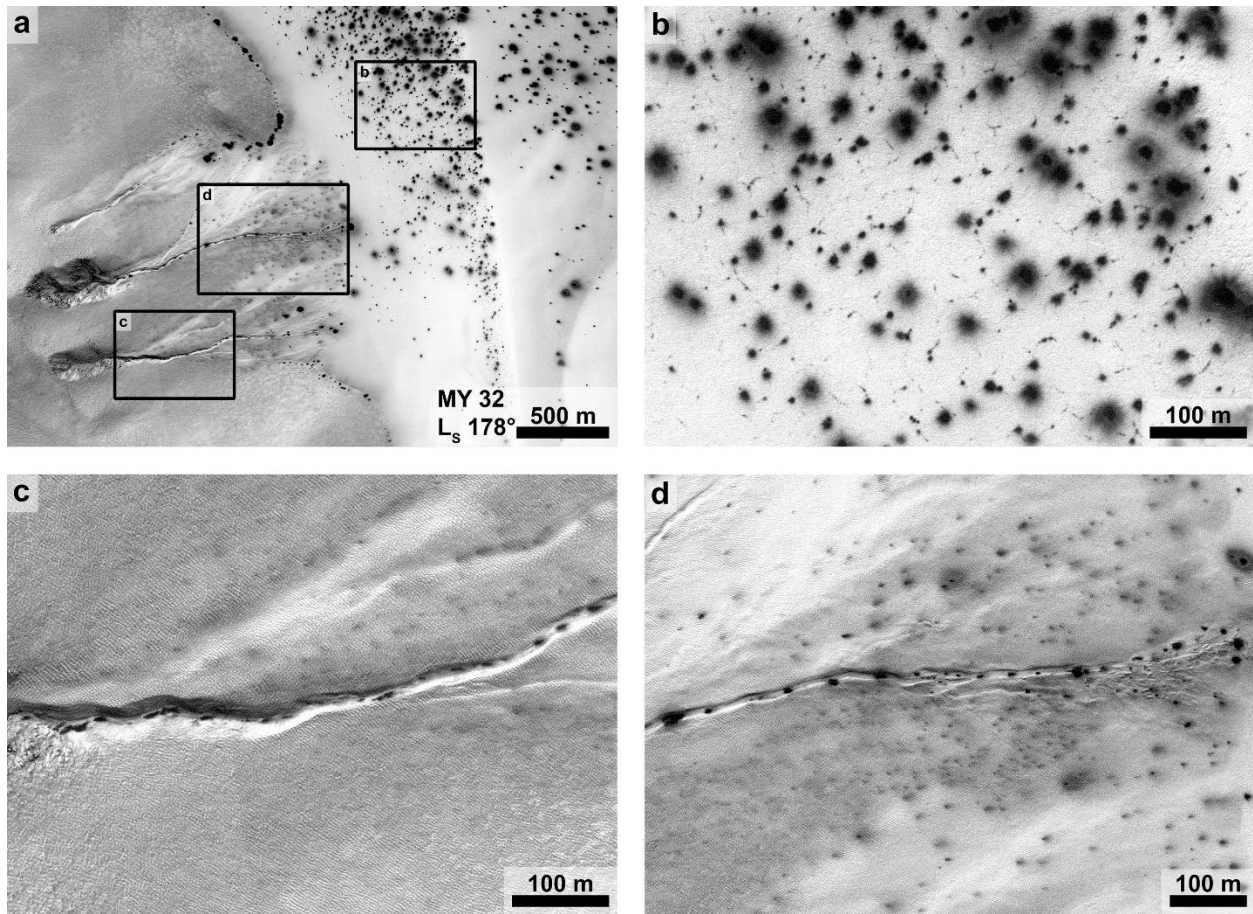


720
 721 **Figure 12:** Diagram of 10 different gullies with contemporary flow-like features activity (except
 722 gully 7 in MY 31, marked with an asterisk, where both activities within the year are related to
 723 block movements), which could be narrowed down to an exact timing within one martian year
 724 based on HiRISE imagery. All gullies are between -68.4° and -70.7° S (see Supplementary Table
 725 01). The activity of the other 26 identified active gullies in the study region could not be
 726 constrained within one martian year. Some of the 10 gullies show periodic activity within different
 727 martian years (y-axis). The crosses represent single HiRISE images, as well as the grey question
 728 marks of gullies 6 to 8 do. However, the question marks represent images where the identification

729 of changes in previous images could not be confirmed due to lower resolutions, atmospheric dust
730 coverage, adverse insolation, and/or extensive surface albedo changes caused by surface
731 defrosting. The blue bars represent the identified surface frost coverage from the beginning of
732 surface frost (beginning of blue bar) to the first image without any identifiable surface frost (end
733 of blue bar). Black bars represent identified activity from between the “before” and “after” HiRISE
734 images.



735
736 **Figure 13:** (a) A gullied slope with adjacent dark dune field in MY 33 during defrosting at the
737 beginning of spring ($L_s 187^\circ$) with numerous dark defrosting spots. (b) The same location after
738 complete defrosting with an ice-free surface during summer ($L_s 349^\circ$). Notice that the dark
739 defrosting spots shown in (a) only occur in regions with a sandy surface (dark dune, windblown
740 sand on the eastern side of the dune, and the gullied slope with preferentially loose material.
741 HiRISE-images (a) EPS_046749_1085 and (b) EPS_050230_1080. North is up in all images.



742

743 **Figure 14:** Examples of dark defrosting spots in the study region. (a) Overview of an east-facing

744 slope with three gullies. The gully aprons run into a dune field, which is within a polar pit. (b)

745 Detail of the dune crest with several dark defrosting spots as well as visible cracks in the slab ice.

746 The image was taken at the end of winter/beginning of spring (Ls 178°) and the dune appears

747 bright probably due to redeposition of CO₂ frost on top on the translucent seasonal CO₂ slab ice

748 cover (comparable to dune field in Figure 8). (c) Detail of one of the gully channels and (d) one

749 of the gully channels with adjacent apron. Dark spots are present within the gully channels and on

750 the aprons, while they are absent on the adjacent hillslopes. This could be caused by the lack of

751 fine material on the slopes, a lack of sufficiently sintered slab ice or different thermal contrasts.

752 HiRISE-image ESP_037729_1115. North is up in all images.

753

754 4. Discussion

755 4.1. Dark spots and flow-like streaks

756 Prior and during the activity of the flow-features in the gullies in Sisyphe Cavi the appearance of
757 dark spots and flow-like streaks are observed on the surface, which do not change the topography.
758 To obviate possible confusion we named these small features emanating from dark defrosting spots
759 “dark flow-like streaks”, while “dark flow-like features” refer to the present-day activity of gullies
760 with observable sediment transport. The phenomenon of dark spots was first observed by Cantor
761 et al. (2002) and is well described in the literature (e.g., Piqueux et al., 2003; Kieffer et al., 2006;
762 Horváth et al., 2009; Hansen et al., 2010; Pilorget et al., 2011; Martínez et al., 2012; Jouannic et
763 al., 2019). The dark spots are formed by basal sublimation of seasonal translucent slab-ice (Figure
764 13; e.g., Piqueux et al., 2003; Kieffer et al., 2006). The basal sublimation leads to overpressure
765 under the ice, leading to the formation of cracks within the ice (see Figure 14b; Portyankina et al.,
766 2012). Through these cracks degassing occurs and dust/sand particles are entrained and
767 redeposited on the surface of the ice (e.g., Piqueux et al., 2003; Kieffer et al., 2006; Portyankina
768 et al., 2012) (Figure 13, 14). If the surface is inclined, the sediment can move downslope forming
769 dark flow-like streaks (e.g., Horváth et al., 2009; Kereszturi et al., 2009, 2010, 2011; Gardin et al.,
770 2010; Hansen et al., 2010, 2012; Jouannic et al., 2019), which are observed in our study region
771 during spring. Within the study region, dark spots are only observed on dark dunes and on gullies
772 (non-active and active ones), particularly within the gully channel and on aprons (Figure 14).
773 Based on the same timing of activity and very similar morphologic features (Figure 14), we infer
774 that the same formation mechanism is responsible for the dark spots and flows in the study region,
775 on dunes as well as in gullies. Thus, these two substrates may have similar properties that differ
776 from the surrounding terrain in order to explain the fact that the dark spots/flows are only found

777 on the dunes and gullies. This implies that dunes, gully channels, and aprons are formed of fine
778 grained material such as sand and dust, which can be mobilized. It could also imply that these
779 substrates somehow favor the formation of slab ice and/or the basal heating.

780 Such dark flow-like streaks have been observed on other gullies, notably the linear gullies on the
781 Russell crater megadune (Gardin et al., 2010; Jouannic et al., 2019) and also on classical gullies
782 in Sisyphi Cavi by Dundas et al. (2019) or in the mid-latitudes by Costard et al. (2007). Dundas et
783 al. (2019) presented a gully as an example for defrosting flows in a polar pit gully which was also
784 investigated in our study. They did not detect changes in topography after the flow disappeared.
785 However, our new observations reveal very small topographic changes, probably missed in the
786 Dundas et al. (2019) study due to fewer available HiRISE images.

787

788 **4.2. Dark flow-like features**

789 We have shown that at the very end of defrosting of the seasonal CO₂ surface ice, flow-like features
790 occur, which modify the topography of the gullies in Sisyphi Cavi. These flows run out onto slopes
791 of 10-15° (Figure 8), hence require some degree of fluidization. Similar flow-like features have
792 been observed in gullies imaged in the shadows of impact craters in three craters in the mid-
793 latitudes (32-38° S; Dundas et al., 2019). As a consequence of the less frequent monitoring of
794 gully-sites outside the polar regions, changes observed in mid-latitude martian gullies may also
795 have happened over frost. However, this has not yet been documented in images because they were
796 not captured at the right time and cadence. In contrast to the Sisyphi Cavi gullies, in the mid-
797 latitudes flow-like features were only observed on south-facing slopes. The timing of activity in
798 Sisyphi Cavi coincides with activity associated with linear gullies on martian sand dunes (Pasquon
799 et al., 2016; Jouannic et al., 2019). However, in this case the activity seems to originate from the

800 frosted areas and propagate over unfrosted areas (Diniega et al., 2013; Jouannic et al., 2019) and
801 again this activity is predominantly on south-facing slopes. Classic gullies on sand dunes have a
802 more complex behavior with activity continuing throughout winter (Diniega et al., 2010; Pasquon
803 et al., 2019a,b).

804 The flow-like features occur when the CO₂ seasonal deposit is becoming thin and discontinuous.
805 This is also visible in the thermal datasets (Figure 11) where the temperature variability of the
806 standard deviation during the sublimation phase is very high. This is the case when ice covered
807 and non-ice covered surfaces are measured at the same time.
808 The formation mechanism of dark flows via pressurized debris flows underneath the slab ice
809 proposed by Pilorget and Forget (2016) is unlikely in Sisyphy Cavi. Raack et al. (2015) showed
810 with spectral and thermal investigations and numerical modelling that the dark flows are on top of
811 the ice and not underneath it, at least for the most active gully in Sisyphi Cavi and our additional
812 image observations support this earlier work.

813 Instead, a modified Cedillo-Flores et al. (2011) model where relatively hot sediments are
814 transported by sublimation of the CO₂ ices underneath the flow seems a more likely scenario. The
815 fact that the deposits are preserved into the summer months leads us to the conclusion that either
816 the underlying CO₂ surface frost is relatively thin and/or the dark flows are turbulent and consist
817 of a mixture of some ice and dry material, which erodes the underlying thin surface frost. If large
818 quantities of CO₂ ice were located either under or within the transported debris, their subsequent
819 sublimation would disturb and change the morphology of the deposits over time. De Haas et al.
820 (2019) calculated that only very small volumetric fractions of CO₂ (<<1%) are required to fluidize
821 a flow, hence a thin surface frost should be adequate to fluidize the flow.

822 The number of active gullies in Sisyphi Cavi is a small proportion of the whole population: 7 of
823 25 sites are active, i.e., only 35 of 2,067 individual gullies on multi-temporal HiRISE-images
824 (about 1.7 %). This value is even lower when only flow-like features without block movements
825 are included ($n = 22$, which is about 1 %). Even though some of the gullies are active annually,
826 many only showed one or two events during the time of image acquisition. This shows that
827 contemporary activity of gullies in this region is rare. To-date, about 35 % of all gullies in the
828 study region have multi-temporal coverage. Some of them only have coverage by two multi-
829 temporal images, which makes a visual identification of changes even more challenging.

830 Active gullies in Sisyphi Cavi could have long recurrence times, similar to debris flows on Earth
831 (e.g., de Haas et al., 2015), but a longer baseline of observation would be needed to substantiate
832 this hypothesis. We found no topographic or other factor (e.g., differential movement of the
833 headwall) that could explain why certain gullies are active (often repeatedly) and others are not,
834 even within those gullies located at the same site. Similarly to debris flows, such events could be
835 limited by the union of sufficient accumulation of loose material (via jetting processes like dark
836 spots/flows?) and rare climatic events that put the system in motion. We now consider whether the
837 activity seen today, integrated over a long time period, could be sufficient to explain the whole
838 gully population in Sisyphi Cavi. The flow-like features that we observed have a sufficient runout
839 to transport material to the base of the gully-fans, hence are capable of explaining the spatial extent
840 of the gullies. Taking into account imaging bias, the flow-like features we observed have a range
841 and variety of orientations that suggest similar events could occur on the whole range of slope
842 orientations in Sisyphi Cavi, although more data would be needed in the under-imaged east-facing
843 orientations to verify this (Figure 9).

844 For gullies #1, #2, and #3 we calculated the area covered by deposits during the time of
845 observation, which ranged between ~600 and ~2,800 m² per MY. Conservatively assuming a 0.5
846 m thickness for these deposits (Raack et al., 2015) results in volumes of between ~300 and ~1,400
847 m³ per MY. We used the publicly available HiRISE DTM derived from the stereo pair
848 ESP_013097_1115 and ESP_013585_1115 to measure the alcove volumes of the gullies. We
849 removed / masked the values of the DTM inside 19 alcoves and linearly interpolated over the gap
850 then differenced with the original DTM (e.g., Conway and Balme, 2014) to find alcove volumes
851 between 32,000 and 2,819,000 m³ (average 956,000 m³). Assuming a constant rate of activity, we
852 find that whole gullies could be formed in decades to several tens of thousands of Mars years
853 (~4,000 Mars years for an average alcove with an average level of activity). As cycles of obliquity
854 have a dominant frequency of 120 ka, eccentricity 95 ka, and precession 51 ka (Ward, 1974; 1979;
855 1992), our estimated gully formation times fall into times when the climate would not have differed
856 substantially from the present-day climate. Hence, it is realistic that processes similar to those
857 active at the present-day could explain the formation of the entire gully-landform without invoking
858 other mechanisms. However, some gully alcoves are filled with presumably aeolian sedimented
859 ice-rich mantle material (e.g., Mustard et al, 2001; Raack et al., 2012; Figure 5). This ice-rich
860 mantle appears uncratered and other studies estimated maximum ages of ~20 Ma for mid-
861 latitudinal locations (Raack et al., 2012) and ~3-5 Ma near the poles (55-60° S) (Willmes et al.,
862 2012). This suggests that gully formation has been ongoing over much longer timescales than
863 recorded by the most recent active gullies, but could still be dependent on conditions similar to the
864 present-day for their formation (indeed conditions conducive for mantle emplacement seem to be
865 non-conducive for gully-formation).

866

867 **4.3. Block movements**

868 We could only constrain the timing of one of the 16 block movements observed during spring,
869 prior to the activity of the flow-like features. Block movements were sometimes spatially
870 associated with and sometimes independent of the flow-like features we observed. All movements
871 occurred in the alcove areas of the gullies where slopes are typically $> 20^\circ$ (Figure 8) and were
872 usually of a few meters, leaving no track. Sometimes the block just moved ~ 1 -2 meters, consistent
873 with just toppling over. It is tempting to link these movements to the flows associated with the
874 gullies, yet no blocks are found in the deposits and similar block movements have been reported
875 in areas without gullies. Dundas et al. (2019) found block movements of meters to tens of meters
876 on slopes of typically 25 - 35° in craters in the northern hemisphere of which the majority occurred
877 in winter and two occurred in summer. Dundas et al. (2019) argued that because similar block
878 movements are not observed at equatorial latitudes, some aspect of the seasonal cycle encourages
879 these types of movement. They suggested that thermal contraction/expansion of underlying ground
880 ice could disturb blocks or even slight changes in the ground ice distribution driven by seasonal
881 temperature changes. They considered loading or other disturbances by the seasonal ice as less
882 likely because some movements were observed in summer. Given that we only have the timing for
883 one of the movements in our dataset, it is currently impossible to move beyond the hypotheses
884 suggested by Dundas et al. (2019).

885

886 **5. Conclusions**

887 Based on various visual and thermal remote sensing data, especially high-resolution multi-
888 temporal images, we identified and analyzed multiple contemporary active gullies within Sisyphi
889 Cavi. On the basis of our study we conclude:

- 890 (1) At least ~1.7 % of all gullies observed with HiRISE show present-day activity (flow-like
891 features and/or block movements). This is a minimum value as some activity could be
892 overlooked and the required number of multi-temporal images for a complete investigation
893 in all martian years is not available for all regions. Nevertheless, the number of active flow-
894 like features (about 1 % of all investigated gullies) is very low which shows that
895 contemporary gully activity in Sisyphi Cavi is generally rare.
- 896 (2) All observed gully activity took place during the end of spring at the end of the seasonal
897 defrosting. During this season, the highest surface temperatures for a partially ice-covered
898 surface were observed. During this time, dark defrosting spots on dunes and gullies were
899 most prevalent.
- 900 (3) The origin of the transported material are the alcoves and small layers on the flanks of gully
901 channels. We made the first observations of headwall erosion of gully alcoves. Material
902 accumulated within the gully channel and moved down in one catastrophic flow event.
- 903 (4) The preferred triggering mechanism for present-day gully activity in Sisyphi Cavi are flows
904 of dry material over seasonal slab ice (comparable to dark spots/flows). It is possible, that
905 the material flowing on top of the ice eroded the underlying ice and formed a mixture of
906 dry material and ice, which was then transported together downslope, fluidizing the flow.
907 It is estimated that the ice thickness at the time of dark flow-like feature appearance was
908 relatively thin, which is consistent with the observation that this activity is linked to the
909 last defrosting stages. The triggering factor of the movement of blocks remains unclear due
910 to the lack of multi-temporal images.
- 911 (5) We found the orientation of active gullies to be broadly consistent with the general
912 population and using volume balance arguments, calculated that some of the active gullies

913 could have been formed within decades to several tens of thousands of MY. This implies
914 that the gullies in Sisyphi Cavi could have been formed in their entirety by processes
915 similar to these active at the present day.

916

917 **Acknowledgments**

918 JR and TH are funded by the German Aerospace Agency (DLR) by the Grant #50QM1801. SJC
919 is grateful to the French Space Agency CNES for funding her HiRISE and CaSSIS related work.
920 AJ is funded by the Swedish National Space Agency SNSA. We thank Dennis Reiss for many
921 fruitful discussions in the initial stage of this survey. The used DIC code is open-source and can
922 be downloaded from: https://github.com/bickelmps/DIC_FFT_ETHZ. We are grateful for very
923 constructive reviews from J. Dickson and an anonymous expert.

924

925 **References**

926 Ayoub, F., Leprince, S., Avouac, J.-P., 2009. Co-Registration and correlation of aerial photographs
927 for ground deformation measurements. *ISPRS J. Photogramm. Remote Sens.* 64, 551 – 560.
928 <https://doi.org/10.1016/j.isprsjprs.2009.03.005>.

929

930 Beyer, R.A., Alexandrov, O., McMichael, S., 2018. The Ames Stereo Pipeline: NASA's Open
931 Source Software for Deriving and Processing Terrain Data. *Earth Space Sci.* 5 (9), 537-548.
932 <https://doi.org/10.1029/2018EA000409>.

933

934 Bickel, V.T., Manconi, A., Amann, F., 2018. Quantitative assessment of digital image correlation
935 methods to detect and monitor surface displacements of large slope instabilities. *Remote*
936 *Sens.* 10, 865. <https://doi.org/10.3390/rs10060865>.

937

938 Bridges, N.T. et al., 2012. Earth-like sand fluxes on Mars. *Nature* 485, 339-342.
939 <https://doi.org/10.1038/nature11022>.

940

941 Cantor, B., Malin, M., Edgett, K.S., 2002. Multiyear Mars Orbiter Camera (MOC) observations
942 of repeated Martian weather phenomena during the northern summer season. *J. Geophys.*
943 *Res.* 107 (E3), 5014. <https://doi.org/10.1029/2001JE001588>.

944

945 Casu, F., Manconi, A., Pepe, A., Lanari, R., 2011. Deformation Time-Series Generation in Areas
946 Characterized by Large Displacement Dynamics: The SAR Amplitude Pixel-Offset SBAS
947 Technique. *Trans. Geosci. Remote Sens.* 49, 7, 2752-2763.
948 <https://doi.org/10.1109/TGRS.2010.2104325>.

949

950 Cedillo-Flores, Y., Treiman, A.H., Lasue, J., Clifford, S.M., 2011. CO₂ gas fluidization in the
951 initiation and formation of martian polar gullies. *Geophys. Res. Lett.* 38, L21202.
952 <https://doi.org/10.1029/2011GL049403>.

953

954 Christensen, P.R. et al., 2001. Mars Global Surveyor Thermal Emission Spectrometer experiment:
955 Investigation description and surface science results. *J. Geophys. Res.* 106 (E10), 23823–
956 23872. <https://doi.org/10.1029/2000JE001370>.

957

958 Christensen, P.R. et al., 2004. The Thermal Emission Imaging System (THEMIS) for the Mars
959 2001 Odyssey mission. *Space Sci. Rev.* 110, 85-130.
960 <https://doi.org/10.1023/B:SPAC.0000021008.16305.94>.

961

962 Conway, S.J. and Balme, M.R., 2014. Decameter thick remnant glacial ice deposits on Mars.
963 *Geophys. Res. Lett.*, 41(15), 5402-5409. <https://doi.org/10.1002/2014GL060314>.

964

965 Conway, S.J., Lamb, M.P., Balme, M.R., Towner, M.C., Murray, J.B., 2011. Enhanced runout and
966 erosion by overland flow at low pressure and sub-freezing conditions: Experiments and
967 application to Mars. *Icarus* 211, 443-457. <https://doi.org/10.1016/j.icarus.2010.08.026>.

968

969 Conway, S.J., Balme, M.R., Kreslavsky, M.A., Murray, J.B., Towner, M.C., 2015. The comparison
970 of topographic long profiles of gullies on Earth to gullies on Mars: A signal of water on
971 Mars. *Icarus* 253, 189-204. <https://doi.org/10.1016/j.icarus.2015.03.009>.

972

973 Conway, S.J., Harrison, T.N., Soare, R.J., Britton, A.W., Steele, L.J., 2019. New slope-normalized
974 global gully density and orientation maps for Mars. *Geol. Soc. London Spec. Publ.* 467, 187-
975 197. <https://doi.org/10.1144/SP467.3>.

976

977 Costard, F., Mangold, N., Baratoux, D., Forget, F., 2007. Current Gully Activity: Dry Avalanches
978 at Seasonal Defrosting as Seen on HiRISE Images. Seventh International Conference on
979 Mars, Contrib. No. 3133.

980
981
982
983
984
985
986
987
988
989
990
991
992
993
994
995
996
997
998
999
1000
1001
1002

de Haas, T. et al., 2015. Earth-like aqueous debris-flow activity on Mars at high orbital obliquity in the last million years. *Nat. Comm.* 6, 7543. <https://doi.org/10.1038/ncomms8543>.

de Haas, T. et al., 2019. Initiation and flow conditions of contemporary flows in Martian gullies. *J. Geophys. Res.: Planets* 124(8), 2246-2271. <https://doi.org/10.1029/2018JE005899>.

Dickson, J.L. and Head J.W., 2009. The formation and evolution of youthful gullies on Mars: Gullies as the late-stage phase of Mars' most recent ice age. *Icarus* 204, 63-86. <https://doi.org/10.1016/j.icarus.2009.06.018>.

Dickson, J.L., Head, J.W., Kreslavsky, M., 2007. Martian gullies in the southern mid-latitudes of Mars: Evidence for climate-controlled formation of young fluvial features based upon local and global topography. *Icarus* 188, 315-323. <https://doi.org/10.1016/j.icarus.2006.11.020>.

Dickson, J.L., Kerber, L.A., Fassett, C.I., Ehlmann, B.L., 2018. A global, blended CTX mosaic of Mars with vectorized seam mapping: A new mosaicking pipeline using principles of non-destructive image editing. 49th Lunar and Planetary Science Conference, Contrib. No. 2083.

Diniega, S., Byrne, S., Bridges, N.T., Dundas, C.M., McEwen, A.S., 2010. Seasonality of present-day Martian dune-gully activity. *Geology* 38, 11, 1047-1050. <https://doi.org/10.1030/G31287.1>.

1003 Diniega, S. et al., 2013. A new dry hypothesis for the formation of martian linear gullies. *Icarus*
1004 225, 526-237. <http://dx.doi.org/10.1016/j.icarus.2013.04.006>.
1005

1006 Dundas, C.M., McEwen, A.S., Diniega, S., Byrne, S., Martinez-Alonso, S., 2010. New and recent
1007 gully activity on Mars as seen by HiRISE. *Geophys. Res. Lett.* 37, L07202,
1008 <https://doi.org/10.1029/2009GL041351>.
1009

1010 Dundas, C.M., Diniega, S., Hansen, C.J., Byrne, S., McEwen, A.S., 2012. Seasonal activity and
1011 morphological changes in martian gullies. *Icarus* 220, 124-143.
1012 <http://dx.doi.org/10.1016/j.icarus.2012.04.005>.
1013

1014 Dundas, C.M., Diniega, S., McEwen, A.S., 2015. Long-term monitoring of martian gully
1015 formation and evolution with MRO/HiRISE. *Icarus* 251, 244-263.
1016 <http://dx.doi.org/10.1016/j.icarus.2014.05.013>.
1017

1018 Dundas, C.M. et al., 2019. The formation of gullies on Mars today. *Geol. Soc. London Spec. Publ.*
1019 467, 67-94. <https://doi.org/10.1144/SP467.5>.
1020

1021 Gardin, E., Allemand, P., Quantin, C., Thollot, P., 2010. Defrosting, dark flow features, and dune
1022 activity on Mars: Example in Russell crater. *J. Geophys. Res.* 115, E06016.
1023 <https://doi.org/10.1029/2009JE003515>.
1024

1025 Ghatan, G.J. and Head, J.W., 2002. Candidate subglacial volcanoes in the south polar region of
1026 Mars: Morphology, morphometry, and eruption conditions. *J. Geophys. Res.* 107.
1027 <https://doi.org/10.1029/2001JE001519>.

1028

1029 Grindrod, P.M., Hollingsworth, J., Ayoub, F., Hunt, S.A., 2018. The Search for Active Marsquakes
1030 Using Subpixel Coregistration and Correlation: Best Practice and First Results. *J. Geophys.*
1031 *Res. Planet* 123, 1881-1900. <https://doi.org/10.1029/2018JE005649>.

1032

1033 Hansen, C.J. et al., 2010. HiRISE observations of gas sublimation-driven activity in Mars'
1034 southern polar regions: I. Erosion of the surface. *Icarus* 205, 283-295.
1035 <https://doi.org/10.1016/j.icarus.2009.07.021>.

1036

1037 Hansen, C.J. et al., 2012. Observations of the northern seasonal polar cap on Mars: I. Spring
1038 sublimation activity and processes. *Icarus* 225, 881-897.
1039 <https://doi.org/10.1016/j.icarus.2012.09.024>.

1040

1041 Harrison, T.N., Osinski, G.R., Tornabene, L.L., Jones, E., 2015. Global documentation of gullies
1042 with the Mars Reconnaissance Orbiter Context Camera and implications for their formation.
1043 *Icarus* 252, 236-254. <https://doi.org/10.1016/j.icarus.2015.01.022>.

1044

1045 Head, J.W., 2000. Tests for ancient polar deposits on Mars: Assessment of morphology and
1046 topographic relationships of large pits (Angusti and Sisyphi Cavi) using MOLA data. *Lunar*
1047 *Planet. Sci.* XXXI, abstract 1118.

1048

1049 Heid, T. and Kääb, A., 2012. Evaluation of existing image matching methods for deriving glacier
1050 surface displacements globally from optical satellite imagery. *Remote Sens. Environ.* 118,
1051 339-355. <https://doi.org/10.1016/j.rse.2011.11.024>.

1052

1053 Herny, C. et al., 2019. Downslope sediment transport by boiling liquid water under Mars-like
1054 conditions: experiments and potential implications for Martian gullies. *Geol. Soc. London*
1055 *Spec. Publ.* 467, 373-410. <https://doi.org/10.1144/SP467.10>.

1056

1057 Heyer, T. et al., 2018. The Multi-Temporal Database of Planetary Image Data (MUTED): A web-
1058 based tool for studying dynamic Mars. *Planet. Space Sci.* 159, 56-65.
1059 <https://doi.org/10.1016/j.pss.2018.04.015>.

1060

1061 Hoffman, N., 2002. Active polar gullies on Mars and the role of carbon dioxide. *Astrobiology* 2,
1062 313-323. <https://doi.org/10.1089/153110702762027899>.

1063

1064 Horváth, A. et al., 2009. Analysis of Dark Albedo Features on a Southern Polar Dune Field on
1065 Mars. *Astrobiology* 9, 90-103. <https://doi.org/10.1089/ast.2007.0212>.

1066

1067 Howard, A.D., 1981. Etched plains and braided ridges of the south polar region of Mars: Features
1068 produced by basal melting of ground ice? NASA Technical Memorandum 84211,
1069 Washington DC, p286.

1070

1071 Hugenholtz, C.H., 2008. Frosted granular flow: a new hypothesis for mass wasting in Martian
1072 gullies. *Icarus* 197, 65-72. <https://doi.org/10.1016/j.icarus.2008.04.010>.
1073

1074 Ishii, T. and Sasaki, S., 2004. Formation of recent martian gullies by avalanches of CO₂ frost.
1075 *Lunar Planet. Sci.* XXXV, abstract 1556.
1076

1077 Ishii, T. et al., 2006. Constraints on the formation of gullies on Mars: a possibility of the formation
1078 of gullies by avalanches of granular CO₂ ice particles. *Lunar Planet. Sci.* XXXVII, abstract
1079 1646.
1080

1081 Jaumann, R. et al., 2007. The high-resolution stereo camera (HRSC) experiment on Mars Express:
1082 Instrument aspects and experiment conduct from interplanetary cruise through the nominal
1083 mission. *Planet. Space Sci.* 55, 928-952. <https://doi.org/10.1016/j.pss.2006.12.003>.
1084

1085 Jouannic, G. et al., 2012. Morphological and mechanical characterization of gullies in a periglacial
1086 environment: The case of the Russell crater dune (Mars). *Planet. Space Sci.* 71, 38-54.
1087 <http://dx.doi.org/10.1016/j.pss.2012.07.005>.
1088

1089 Jouannic, G. et al., 2019. Morphological characterization of landforms produced by springtime
1090 seasonal activity on Russel Crater megadune, Mars. *Geol. Soc. London Spec. Publ.* 467,
1091 115-144. <https://doi.org/10.1144/SP467.16>.
1092

1093 Kereszturi, A. et al., 2009. Recent rheologic processes on dark polar dunes of Mars: Driven by
1094 interfacial water? *Icarus* 201, 492-503. <https://doi.org/10.1016/j.icarus.2009.01.014>.
1095

1096 Kereszturi, A. et al., 2010. Indications of brine related local seepage phenomena of the northern
1097 hemisphere of Mars. *Icarus* 207, 149-164. <https://doi.org/10.1016/j.icarus.2009.10.0142>.
1098

1099 Kereszturi, A., Vincendon, M., Schmidt, F., 2011. Water ice in the dark dune spots of Richardson
1100 crater on Mars. *Planet. Space Sci.* 59, 26-42. <https://doi.org/10.1016/j.pss.2010.10.015>.
1101

1102 Kieffer, H.H., Christensen, P.R., Titus, T.N., 2006. CO₂ jets formed by sublimation beneath
1103 translucent slab ice in Mars' seasonal south polar cap. *Nature* 772, 793-796.
1104 <https://doi.org/10.1038/nature04945>.
1105

1106 Kirk, R.L. et al., 2008. Ultrahigh resolution topographic mapping of Mars with MRO HiRISE
1107 stereo images: Meter-scale slopes of candidate Phoenix landing sites. *J. Geophys. Res.* 113,
1108 E00A24. <https://doi.org/10.1029/2007JE003000>.
1109

1110 Malin, M.C. and Edgett, K.S., 2000. Evidence for Recent Groundwater Seepage and Surface
1111 Runoff on Mars. *Science* 288, 2330. <https://doi.org/10.1126/science.288.5475.2330>.
1112

1113 Malin, M.C., Edgett, K.S., Posiolova, L.V., McColley, S.M., Noe Dobrea, E.Z., 2006. Present-
1114 Day Impact Cratering Rate and Contemporary Gully Activity on Mars. *Science* 314, 1573.
1115 <https://doi.org/10.1126/science.1135156>.

1116

1117 Malin, M.C. et al., 2007. Context camera investigation on board the Mars Reconnaissance Orbiter.

1118 J. Geophys. Res. 112, E05S04. <https://doi.org/10.1029/2006JE002808>.

1119

1120 Martínez, G.M. and Renno, N.O., 2013. Water and Brines on Mars: Current Evidence and

1121 Implications for MSL. Space Sci. Rev. 175, 29-51. <https://doi.org/10.1007/s11214-012->

1122 [9956-3](https://doi.org/10.1007/s11214-012-9956-3).

1123

1124 Martínez, G.M., Renno, N.O., Elliott, H.M., 2012. The evolution of the albedo of dark spots

1125 observed on Mars polar region. Icarus 221, 816-830.

1126 <https://doi.org/10.1016/j.icarus.2012.09.008>.

1127

1128 McEwen, A.S. et al., 2007a. A Closer Look at Water-Related Geologic Activity on Mars. Science

1129 317, 5848, 1706-1709. <https://doi.org/10.1126/science.1143987>.

1130

1131 McEwen, A.S. et al., 2007b. Mars Reconnaissance Orbiter's High Resolution Imaging Science

1132 Experiment (HiRISE). J. Geophys. Res. 112, E05S02.

1133 <https://doi.org/10.1029/2005JE002605>.

1134

1135 Murray, B.C. et al., 1972. Geological framework of the south polar region of Mars. Icarus 17 (2),

1136 328-345. [https://doi.org/10.1016/0019-1035\(72\)90004-8](https://doi.org/10.1016/0019-1035(72)90004-8).

1137

1138 Musselwhite, D.S., Swindle, T.D., Lunine, J.I., 2001. Liquid CO₂ Breakout and the Formation of
1139 Recent Small Gullies on Mars. *Geophys. Res. Lett.* 28, 7, 1283-1285.
1140 <https://doi.org/10.1029/2000GL012496>.
1141

1142 Mustard, J.F., Cooper, C.D., Rifkin, M.K., 2001. Evidence for recent climate change on Mars from
1143 the identification of youthful near-surface ground ice. *Nature* 412, 411-414.
1144 <https://doi.org/10.1038/35086515>.
1145

1146 Pasquon, K., Gargani, J., Massé, M., Conway, S.J., 2016. Present-day formation and seasonal
1147 evolution of linear dune gullies on Mars. *Icarus* 274, 195-210.
1148 <http://dx.doi.org/10.1016/j.icarus.2016.03.024>.
1149

1150 Pasquon, K., et al., 2019a. Are different Martian gully morphologies due to different processes on
1151 the Kaiser dune field? *Geol. Soc. London Spec. Publ.* 467, 145-164.
1152 <https://doi.org/10.1144/SP467.13>.
1153

1154 Pasquon, K. et al., 2019b. Present-day development of gully-channel sinuosity by carbon dioxide
1155 gas supported flows on Mars. *Icarus* 329, 296-313.
1156 <https://doi.org/10.1016/j.icarus.2019.03.034>.
1157

1158 Pilorget, C. and Forget, F., 2016. Formation of gullies on Mars by debris flows triggered by CO₂
1159 sublimation. *Nat. Geosci.* 9, 65-69. <https://www.nature.com/articles/ngeo2619>.
1160

1161 Pilorget, C., Forget, F., Millour, E., Vincendon, M., Madeleine, J.B., 2011. Dark spots and cold
1162 jets in the polar regions of Mars: New clues form a thermal model of surface CO₂ ice. *Icarus*
1163 213, 131-149. <https://doi.org/10.1016/j.icarus.2011.01.031>.
1164

1165 Piqueux, S., Byrne, S., Richardson, M.I., 2003. Sublimation of Mars's southern seasonal CO₂ ice
1166 cap and the formation of spiders. *J. Geophys. Res.* 108, E8, 5084.
1167 <https://doi.org/10.1029/2002JE002007>.
1168

1169 Portyankina, G., Pommerol, A., Aye, K.-M., Hansen, C.J., Thomas, N., 2012. Polygonal cracks in
1170 the seasonal semi-translucent CO₂ ice layer in Martian polar areas. *J. Geophys. Res.* 117,
1171 E02006. <https://doi.org/10.1029/2011JE003917>.
1172

1173 Raack, J., Reiss, D., Hiesinger, H., 2012. Gullies and their relationships to the dust-ice mantle in
1174 the northwestern Argyre Basin, Mars. *Icarus* 219, 129-141.
1175 <https://doi.org/10.1016/j.icarus.2012.02.025>.
1176

1177 Raack, J. et al., 2015. Present-day seasonal gully activity in a south polar pit (Sisyphi Cavi) on
1178 Mars. *Icarus* 251, 226-243. <https://doi.org/10.1016/j.icarus.2014.03.040>.
1179

1180 Raack, J. et al., 2017. Water induced sediment levitation enhances downslope transport on Mars.
1181 *Nature Comm.* 8, 1151. <https://doi.org/10.1038/s41467-017-01213-z>.
1182

1183 Reiss, D., Erkeling, G., Bauch, K.E., Hiesinger, H., 2010. Evidence for present day gully activity
1184 on the Russell crater dune field, Mars. *Geophys. Res. Lett.* 37, L06203.
1185 <https://doi.org/10.1029/2009GL042192>.
1186

1187 Reiss, D. et al., 2016. Dust Devil Tracks. *Space Sci. Rev.* 203, 143-181.
1188 <https://doi.org/10.1007/s11214-016-0308-6>.
1189

1190 Schorghofer, N. and Edgett, K.S., 2006. Seasonal surface frost at low latitudes on Mars. *Icarus*
1191 180, 321-334. <https://doi.org/10.1016/j.icarus.2005.08.022>.
1192

1193 Schorghofer, N, Aharonson, O., Gerstell, M.F. Tatsumi, L., 2007. Three decades of slope streak
1194 activity on Mars. *Icarus* 191, 132-140. <https://doi.org/10.1016/j.icarus.2007.04.026>.
1195

1196 Sharp, R.P., 1973. Mars: South polar pits and etched terrain. *J. Geophys. Res.* 78 (20), 4222-4230.
1197 <https://doi.org/10.1029/JB078i020p04222>.
1198

1199 Steward, S.T. and Nimmo, F., 2002. Surface runoff features on Mars: Testing the carbon dioxide
1200 formation hypotheses. *J. Geophys. Res.* 107 (E9), 5069.
1201 <https://doi.org/10.1029/2000JE001465>.
1202

1203 Tanaka, K.L. and Scott, D.H., 1987. Geologic map of the polar regions of Mars. USGS Map I-
1204 1802C. <https://doi.org/10.3133/i1802C>.
1205

1206 Thomas, N., Portyankina, G., Hansen, C. J., Pommerol, A., 2011. HiRISE observations of gas
1207 sublimation-driven activity in Mars' southern polar regions: IV. Fluid dynamics models of
1208 CO₂ jets. *Icarus* 212, 66-85. <https://doi.org/10.1016/j.icarus.2010.12.016>
1209

1210 Thomas, N. et al., 2017. The Colour and Stereo Surface Imaging System (CaSSIS) for the ExoMars
1211 Trace Gas Orbiter. *Space Sci. Rev.* 212, 1897. <https://doi.org/10.1007/s11214-017-0421-1>.
1212

1213 Thomas, P., Squyres, S., Herkenhoff, K., Howard, A., Murray, B., 1992. Polar deposits of Mars.
1214 In *Mars*, ed. H.H. Kieffer, B.M. Jakosky, C.W. Snyder, M.S. Matthews. Tuscon, AZ:
1215 University of Arizona Press, pp. 767-795.
1216

1217 Vincendon, M. et al., 2010a. Near-tropical subsurface ice on Mars. *Geophys. Res. Lett.* 37,
1218 L01202. <https://doi.org/10.1029/2009GL041426>.
1219

1220 Vincendon, M., Forget, F., Mustard, J., 2010b. Water ice at low to midlatitudes on Mars. *J.*
1221 *Geophys. Res.* 115, E10001. <https://doi.org/10.1029/2010JE003584>.
1222

1223 Ward, W.R., 1974. Climatic variations on Mars:1. Astronomical theory of insolation. *J. Geophys.*
1224 *Res.* 79, 3375-3386. <https://doi.org/10.1029/JC079i024p03375>.
1225

1226 Ward, W.R., 1979. Present obliquity oscillations of Mars: Fourth-order accuracy in orbitale e and
1227 I. *J. Geophys. Res.* 84, 237-241. <https://doi.org/10.1029/JB084iB01p00237>.
1228

1229 Ward, W.R., 1992. Long-term orbital and spin dynamics of Mars, in Mars, edited by H.H. Kieffer
1230 et al., chap. 9, 298-320, Univ. of Ariz. Press, Tucson.

1231

1232 Willmes, M., Reiss, D., Hiesinger, H., Zanetti, M., 2012. Surface age of the ice-dust mantle deposit
1233 in Malea Planum, Mars. Planet. Space Sci. 60, 199-206.
1234 <https://doi.org/10.1016/j.pss.2011.08.006>.

1235

1236 Zuber, M.T. et al., 1992. The Mars Observer laser altimeter investigation. J. Geophys. Res. 97
1237 (E5), 7781–7797. <https://doi.org/10.1029/92JE00341>.

1238

1239

Present-day gully activity in Sisyphi Cavi, Mars – Flow-like features and block movements

Jan Raack^a, Susan J. Conway^b, Thomas Heyer^a, Valentin T. Bickel^{c,d}, Meven Philippe^b, Harald Hiesinger^a, Andreas Johnsson^e, Marion Massé^b

^aInstitut für Planetologie, Westfälische Wilhelms-Universität Münster, Wilhelm-Klemm-Str. 10, 48149 Münster, Germany

^bLaboratoire de Planétologie et Géodynamique, UMR 6112, CNRS, Université de Nantes, 2 chemin de la Houssinière, BP 92205, 44322 Nantes Cedex 3, France

^cDepartment Planets and Comets, Max-Planck-Institute for Solar System Research, Justus-von-Liebig-Weg 3, 37077 Göttingen, Germany

^dDepartment of Earth Sciences, ETH Zurich, Sonneggstrasse 5, 8092 Zurich, Switzerland

^eDepartment of Earth Sciences, University of Gothenburg, Box 460, Gothenburg SE-405 30, Sweden

Supplementary Material

Supplementary Table 01: List of all identified active gullies with associated region, specific coordinates, orientation, short description, and time of activity in the study region.

Gully	Region	Lon. (E) / Lat. (S)	Orientation	Description	Year active	Time span between activity
Gully 1	5	1.285° / -68.471°	109°	Large dark flow (Figure 3)	MY 33	26 sols
Gully 2	5	1.23° / -68.481°	113°	Dark flow	MY 29 MY 30 MY 31 MY 32 MY 33	31 sols 91 sols 27 sols 38 sols 26 sols
Gully 3	5	1.443° / -68.537°	352°	Large dark flow (Figure 5 and Raack et al., 2015)	MY 29 MY 30 MY 31	27 sols 91 sols 17 sols
Gully 4	5	1.68° / -68.512°	321°	Small dark flow	MY 28-31	2012 sols
Gully 5	10	-13.84° / -69.48°	232°	Small flow	MY 32	42 sols
Gully 6	10	-13.835° / -69.481°	200°	Very small changes	MY 31 MY 32 MY 33	33 sols 42 sols 65 sols
Gully 7	10	-13.826° / -69.493°	224°	Very small changes plus block movements [†]	MY 31 [†] MY 31 [†] MY 33	65 sols 16 sols 54 sols
Gully 8	10	-13.786° / -69.512°	198°	Very small changes	MY 31 MY 32	33 sols 133 sols
Gully 9	10	-13.71° / -69.525°	196°	Several small changes	MY 33	44 sols
Gully 10	10	-13.698° / -69.527°	208°	Some small changes	MY 32 MY 33	42 sols 44 sols
Gully 11	11	1.2° / -70.92°	216°	Largest activity (see Figure 4)	MY 32-33	673 sols
Gully 12	11	1.224° / -70.92°	229°	Very small changes plus large block movement [†] (see Figure 7)	MY 31-32 MY 32-33 [†]	673 sols 673 sols
Gully 13	11	1.392° / -70.949°	194°	Medium changes	MY 32-33	673 sols
Gully 14	12	4.292° / -70.678°	305°	Small dark flow	MY 32-33 MY 33	575 sols 166 sols
Gully 15	12	4.21° / -70.74°	297°	Medium dark flow	MY 29-32	2160 sols

Gully 16	14	3.161° / -71.203°	234°	Small changes	MY 32-33	1400 sols
Gully 17	14	3.186° / -71,204°	247°	Very small changes	MY 30-31	708 sols
Gully 18	14	3.205° / -71,212°	260°	Small changes	MY 28-33	3357 sols
Gully 19	14	3.17° / -71.288°	301°	Very small dark flow	MY 28-30	1163 sols
Gully 20	18	2.237° / -72.159°	301°	Medium changes	MY 29-32	2032 sols
Gully 21	18	2.206° / -72.17°	316°	Block movement	MY 29-32	2032 sols
Gully 22	18	2.203° / -72.17°	315°	Block movement	MY 29-32	2032 sols
Gully 23	18	2.193° / -72.175°	325°	Block movement	MY 32-33	634 sols
Gully 24	18	2.189° / -72.176°	262°	Block movement	MY 32-33	634 sols
Gully 25	18	2.19° / -72.177°	300°	Block movement	MY 29-32	2032 sols
Gully 26	18	2.184° / -72.178°	300°	Block movement	MY 29-32	2032 sols
Gully 27	20	3.724° / -72.172°	258°	Block movement	MY 31-33	2688 sols
Gully 28	20	3.724° / -72.173°	222°	Block movement	MY 29-30	709 sols
Gully 29	20	3.725° / -72.175°	293°	Block movement	MY 29-30	709 sols
Gully 30	20	3.745° / -72.182°	209°	Block movement	MY 29-30	613 sols
Gully 31	20	3.898° / -72.244°	255°	Small changes	MY 29-30 MY 30-33	709 sols 1969 sols
Gully 32	20	3.909° / -72.249°	224°	Block movement (in same gully, but different places)	MY 30-33	1969 sols
Gully 33	20	3.914° / -72.248°	236°	Block movement (in same gully, but different places)	MY 30-33	1969 sols
Gully 34	20	3.924° / -72.248°	249°	Small changes plus block movements	MY 30-33	1969 sols
Gully 35	20	3.943° / -72.253°	229°	Block movement	MY 29-30	709 sols

Supplementary Table 02: Slope angles of all investigated gullies in region 5 and 11 from the beginning of their alcoves, through their channels, above their aprons until the end of the general slope (Figure 8). Slope angles are reported as calculated over 100 m-long segments of the gully length. The last row of the table shows the overall average angle of the slope following the path of individual gullies. Active gullies are marked in bold.

Length (m)	Region 11						Region 5									
	A	B	C	D	E	F	G	H	I	J	K	L	M	N	O	P
100	29°	33°	39°	43°	36°	37°	38°	36°	34°	36°	35°	15°	35°	50°	38°	42°
200	36°	45°	34°	38°	35°	32°	28°	29°	27°	26°	27°	15°	37°	44°	38°	31°
300	38°	34°	28°	30°	37°	37°	20°	20°	23°	29°	20°	13°	23°	23°	33°	22°
400	27°	25°	22°	24°	23°	26°	18°	18°	20°	20°	17°	13°	15°	18°	22°	17°
500	21°	21°	19°	19°	19°	14°	16°	15°	18°	19°	16°	12°	14°	14°	15°	16°
600	17°	16°	16°	12°	15°	12°	15°	14°	19°	15°	15°	11°	12°	14°	15°	12°
700	15°	13°	12°	10°	12°	16°	16°	16°	15°	16°	16°	11°	11°	13°	13°	15°
800	14°	12°	11°	11°	12°	11°	16°	16°	14°	15°	14°	12°	11°	13°	16°	15°
900	11°	11°	11°	12°	11°	12°	14°	15°	15°	19°	15°	11°	12°	13°	18°	15°
1000	13°	13°	12°	12°	14°	10°	13°	16°	15°	14°	14°	12°	12°	12°	19°	14°
1100	10°	12°	11°	10°	11°	11°	14°	14°	15°	14°	14°	11°	10°	11°	14°	13°
1200	12°	10°	11°	9°	9°	10°	15°	13°	16°	13°	20°	11°	9°	10°	13°	12°
1300		11°	11°	12°	12°	9°	14°	13°	15°	13°	13°	10°	11°	10°	12°	12°
1400		11°	11°	10°	8°	9°	12°	13°	14°	12°	14°	11°	10°	11°	12°	11°
1500		11°	12°	10°	10°	10°	13°	13°	14°	13°	12°	10°	11°	11°	11°	11°
1600		12°	9°	9°	10°	9°	11°	12°	13°	13°	13°	10°	10°	10°	10°	10°
1700		9°	14°	11°	11°	10°	10°	11°	13°	13°	9°	10°	10°	11°	10°	10°
1800		11°	7°	10°	11°	10°	11°	9°	13°	12°	9°	9°	10°	11°	10°	11°
1900		11°	11°	10°	10°	10°	10°	9°	12°	11°	7°	8°	9°	10°	9°	10°
2000		9°	12°	10°	11°	11°	13°	13°	11°	19°	2°	8°	7°	9°	7°	9°
2100		9°	11°	9°	10°	8°	19°	18°	10°	3°		6°	5°	8°		8°
2200		10°	8°	10°	9°	8°	25°	25°	8°			0°	3°			8°
2300		10°	9°	10°	10°	9°			5°			0°	6°			7°
2400			9°	10°	8°	9°							13°			
2500			8°	9°	9°	8°							12°			
2600			6°	9°	7°	8°										
2700			4°	6°	6°	7°										
2800				4°	3°	6°										
2900						5°										
	20°	16°	14°	14°	14°	13°	16°	16°	16°	16°	16°	10°	13°	16°	17°	14°

Supplementary Table 03: List of the HiRISE image pairs used for DTM generation, including their spatial resolution and their mean intersection error as a measure for DTM quality. Some of the listed DTMs have been used to orthorectify the HiRISE imagery used for DIC.

Timeframe	HiRISE pair	DTM spatial resolution (m/pix)	Mean intersection error (m)
2007 - 2011	ESP_023290_1090 PSP_005621_1090	2	0.62
2007 - 2016	ESP_048608_1090 PSP_005621_1090	1	0.25
2013 - 2015	ESP_030859_1090 ESP_039747_1090	3	0.87
2015 - 2016	ESP_039747_1090 ESP_048608_1090	0.5	0.48